Master Thesis

Study of an Inverse-Kinematics Experiment for Measuring Nuclear De-Excitation Process Following Oxygen-Nucleon Reaction for Improved Neutrino-Nucleus Interaction Prediction
(酸素-核子反応に伴う脱励起過程測定のための逆運動学実験の研究 ―ニュートリノ-原子核反応予測の精密化に向けて―)

January, 2025

Department of Physics, Graduate School of Science
The University of Tokyo
東京大学大学院理学系研究科物理学専攻

Yusuke Mizuno
水野裕介

Abstract

Neutrinos from supernovae offer valuable insights into physics and astrophysics. In particular, the discovery of diffuse supernova neutrino background (DSNB) would pave the way for detailed studies of the supernova explosion mechanism, the evolution of the universe, and the properties of neutrinos themselves. The Super-Kamiokande (SK) is a water Cherenkov detector and currently is the most sensitive neutrino detector in the DSNB energy region.

A barrier to discovering DSNB is the large uncertainties in the neutrino-nucleus interactions between atmospheric neutrinos and oxygen nuclei, particularly the neutral-current quasi-elastic (NCQE) interaction. In order to solve this problem, we will conduct the SAMURAI-79 experiment, an inverse kinematics experiment for measuring the de-excitation process of ^{15}N, ^{15}O, and ^{16}O using the SAMURAI spectrometer at RIBF, RIKEN Nishina Center. We plan to measure the branching ratios of major de-excitation channels as a function of excitation energy of these nuclei.

In this work, we conducted a simulation study for the measurement of ^{15}N. The insights gained from this study will be applied when conducting the SAMURAI-79 experiment. First, we developed a reconstruction method for the excitation energy of ^{15}N using a setup with a newly developed detector. A resolution of 1.6 MeV (σ) in the excitation energy is achieved in this study.

Second, we studied the performance of measuring of residual nuclei and neutrons produced by the de-excitation process. We found that all residual nuclei can be detect by applying a magnetic field of 2.0 T. We found that the evaporation neutrons from $^{15}\mathrm{N} \rightarrow {}^{14}\mathrm{N} + n$ reaction can be detected at a 12% efficiency using the exsisting detectors.

Then, we estimated the expected statistical performance for measuring the branching raitos. The de-excitation channels $^{14}\mathrm{N} + n$ and $^{12}\mathrm{C} + p + n$ can be measured with statistical uncertainties of 0.3% and 2.1%, respectively.

Finally, we examined the expected impact on the DSNB sensitivity at SK by improving the atmospheric neutrino event prediction. Reducing the uncertainties of the atmospheric neutrino event to 10% enable us to discover DSNB at more than 3σ significance.

Acknowledgment

I would like to express my gratitude to all those who supported me.

First of all, I would like to express my sincere gratitude to my supervisor, Prof. Yasuhiro Nakajima, for providing me with the invaluable opportunity to conduct my research. I learned many things under his kind and excellent guidance. I would not have been able to complete this work without his support.

I would like to thank the neutrino physics researchers who worked with me, Prof. Ryosuke Akutsu, Tada-san, Dr. Seisho Abe, Dr. Yosuke Ashida, Prof. Yusuke Koshio, Li-Cheng Feng, and Dr. Masayuki Harada for their support. Their insightful advice, constructive discussions, and continuous support have been essential throughout my research.

I would like to thank the nuclear physics researchers, especially, Dr. Hideaki Otsu, Dr. Tadaaki Isobe, Dr. Yosuke Kondo, Dr. Yuki Kubota, Dr. Seiya Sakai, Dr. Hiroshi Sakurai, Prof. Yukinobu Watanabe, Dr. Shinsuke Nakayama, Prof. Kazuyuki Ogata, and Prof. Futoshi Minato for their support in the area of nuclear physics.

I would like to thank the members of the Yokoyama-Nakajima group, Prof. Masashi Yokoyama, Prof. Kota Nakagiri, Daniel, Yoshimi, Kodama-san, Kobayashi-san, Arai-kun, Goto-kun, Muro-kun, Hayasaki-kun, Masaki-kun, Yufei Kong and Kono-san for their lots of support.

Finally, I would like to express my sincere gratitude to my family. They always supported me for a long time.

Contents

List of Figures

List of Tables

Chapter 1

Introduction

One of the physics goals of Super-Kamiokande is the first observation of Diffuse Supernova Neutrino Background (DSNB). An understanding the neutrino-nucleus interaction is important for observing DSNB. This chapter introduces DSNB and neutrino-nucleus interaction.

1.1 Diffuse Supernova Neutrino Background

1.1.1 Supernova Explosion

A supernova is an intense explosion that occurs when a massive star ends its life. Supernova is one of the most dynamic phenomena in the universe, a kinetic energy of which reaches $\sim 10^{51}$ erg.

There are two explosion mechanisms of supernovae, thermonuclear supernovae and core-collapse supernovae (CCSN). The sources of the energy of these supernovae are the nuclear and gravitational energy for the thermonuclear supernovae and the CCSNe, respectively. Although both types of supernovae emit neutrinos, much more neutrinos are emitted from the CCSNe. Therefore this thesis focuses on the CCSNe.

All four forces, electromagnetic force, strong force, weak force, and gravitation are involved in the supernova dynamics. Currently, theoretical simulations do not perfectly succeed in modeling the explosion. Neutrinos play an essential role in the supernova explosion, carrying 99% of the explosion energy in the CCSNe. The observation of supernova neutrinos is crucial for understanding the supernova explosion mechanism and provides us with many insights into physics and astrophysics.

1.1.2 Neutrino from Supernova

Neutrinos are fundamental particles, neutral leptons with a spin of 1/2. Supernova neutrinos are emitted from supernova explosions. The mechanism of the CCSN and the neutrino emissions is described below [30].

1. Start of gravitational collapse
   A star supports itself against gravity with the pressure produced by nuclear fission. Since an iron nucleus is the most stable, nuclear fission stops when the iron core is formulated. If this happens, no energy is generated in the core and the core pressure does not increase any further. Then the core starts to collapse. As the core collapses, the density and temperature of the core become higher. It promotes the creation of neutrinos by electron capture:

$$e^- + A(N, Z) \to \nu_e + A(N+1, Z-1). \tag{1.1}$$

2. Neutrino trapping
   As the core density increases, the neutrinos are trapped in the core. This region is called the neutrino sphere.

3. Neutronization burst
   When the core density reaches the nucleon density, the collapse stops and an outward shockwave is generated (core-bounce). The shockwave heats the core materials and electron capture processes

$$e^- + p \to \nu_e + n \tag{1.2}$$

   proceed rapidly. Once the shockwave arrives at the neutrino sphere, the emission of neutrinos begins (neutronization burst). The duration of the neutronization burst is $\lesssim 10\,\mathrm{ms}$. The remaining central core stabilizes and forms a proto-neutron star (PNS).

4. PNS cooling
   After the passage of the shockwave, the materials accrete onto the PNS and emit all types of neutrinos via the following processes:

$$e^+ + n \longleftrightarrow \bar{\nu}_e + p, \tag{1.3}$$
$$e^- + e^+ \longleftrightarrow \nu_X + \bar{\nu}_X, \tag{1.4}$$
$$e^\pm + N \longleftrightarrow e^\pm + N + \nu_X + \bar{\nu}_X, \tag{1.5}$$
$$N + N \longleftrightarrow N + N + \nu_X + \bar{\nu}_X, \tag{1.6}$$
$$\gamma \longleftrightarrow \nu_X + \bar{\nu}_X, \tag{1.7}$$
$$\gamma + e^\pm \longleftrightarrow e^\pm + \nu_X + \bar{\nu}_X. \tag{1.8}$$

   When the shockwave reaches the surface of the star, it ejects the outer layer, leaving a neutron star after the explosion.

Figure 1.1 shows the time evolution of neutrino luminosity and the average energy in a numerical simulation [1]. ν_x represents $\nu_x = (\nu_\mu + \bar{\nu}_\mu + \nu_\tau + \bar{\nu}_\tau)/4$. The sharp peak in the ν_e plot in the top figure corresponds to the neutronization burst.

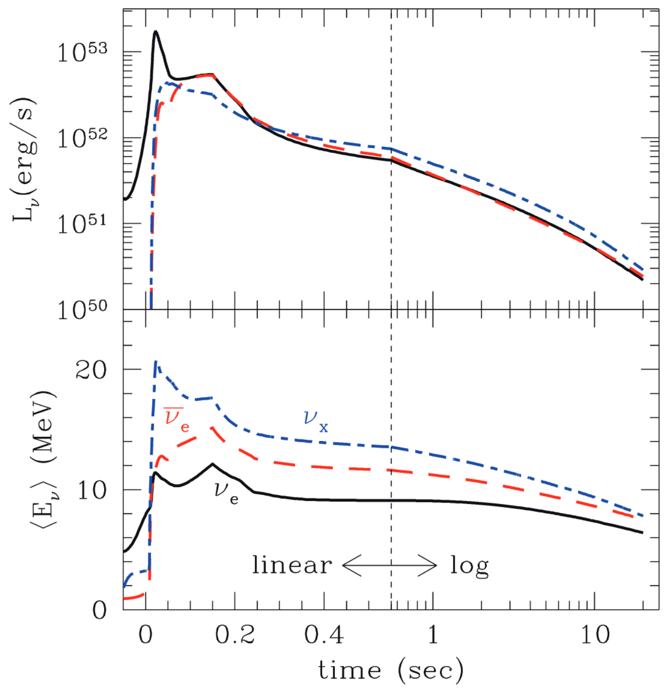

Figure 1.1: Time evolution of the neutrino luminosity and the average energy in a numerical simulation [1].

1.1.3 Diffuse Supernova Neutrino Background

The DSNB is an accumulated flux of neutrinos emitted from all past CCSNe.

The number density of DSNBs which were emitted at redshifts $z \sim z + dz$ and whose energies at emission were $E_\nu \sim E_\nu + dE_\nu$ is expressed as:

$$dn(E_\nu) = R_{\rm CCSN}(z)(1+z)^3 \frac{dt}{dz} dz \frac{dN(E_\nu)}{dE_\nu} dE_\nu, \tag{1.9}$$

where $R_{\rm CCSN}$ is the CCSN rate in a unit comoving volume at redshift z. t is time at redshift z. dN/dE_ν is the number spectrum of neutrinos from each CCSN. At present, the number density of DSNBs is reduced by a factor of $(1+z)^{-3}$ and the energy is also redshifted, scaling as $(1+z)^{-1}$. Therefore, the number density at present is written as:

$$dn(E_\nu) = R_{\rm CCSN}(z) \frac{dt}{dz} dz \frac{dN(E'_\nu)}{dE'_\nu} (1+z) dE_\nu. \tag{1.10}$$

The quantities at the neutrino emisson time is attached with the superscript prime sign. The DSNB flux is the accumulation of all past neutrinos and expressed as:

$$\frac{d\Phi(E_\nu)}{dE_\nu} = c \frac{dn(E_\nu)}{dE_\nu} = c \int_0^\infty R_{\rm CSSN}(z) \frac{dt}{dz} \frac{dN(E'_\nu)}{dE'_\nu} dz, \tag{1.11}$$

where c is the speed of light. As shown in Eq. (1.11), various factors affect the DSNB flux. There are other factors that affect the DSNB flux as described below.

Failed supernovae

Some stars fail in the explosion and become black holes. This phenomenon is called failed supernovae. In this case, the matter accretion continues until black hole formation, and generally requires a longer period than the standard CCSN, and more energetic neutrinos are emitted. Therefore, the rate of failed supernovae contributes to the DSNB flux.

Neutrino oscillation effects

Neutrino oscillation is a phenomenon in which one flavor of neutrino stochastically changes to another flavor with time evolution. For instance, the number spectrum of $\bar{\nu}_e$ is a mixture of spectra of all flavor neutrinos:

$$\frac{dN_{\bar{\nu}_e}}{dE_\nu} = \bar{P}_{ee}\frac{dN'_{\bar{\nu}_e}}{dE_\nu} + \bar{P}_{\mu e}\frac{dN'_{\bar{\nu}_\nu}}{dE_\nu} + \bar{P}_{\tau e}\frac{dN'_{\bar{\nu}_\tau}}{dE_\nu}, \tag{1.12}$$

where $\bar{P}_{\alpha e}\,(\alpha = e, \mu, \tau)$ is the transition probability from $\bar{\nu}_\alpha$ to $\bar{\nu}_e$, satisfying $\sum_\alpha \bar{P}_{\alpha e} = 1$. These probabilities are determined by the properties of neutrinos themselves.

1.1.4 Current Status of DSNB Search

Many theoretical models have been proposed to predict the DSNB flux. Figure 1.2 shows the predicted energy distribution of the DSNB $\bar{\nu}_e$ flux for various models. There is an order of magnitude difference in the flux depending on the model. The observation of DSNB provides us with important information on the evolution of the universe, the mechanism of supernova explosions, and the properties of neutrinos themselves. However, DSNB has not yet been discovered. The signal in experimental searches is usually inverse beta decay with electron antineutrinos ($\bar{\nu}_e$). Currently, the Super-Kamiokande (SK) experiment and the KamLAND experiment provide the most stringent upper limit on the DSNB flux. Figure 1.3 shows the upper limit of the $\bar{\nu}_e$ flux in the latest result [17]. The experimental upper limits are approaching a point where they can be compared with theoretical prediction.

1.2 Neutrino-nucleus Interaction

Except for the gravitational interaction, neutrinos interact with materials only via weak boson exchanges (weak interaction). Depending on the weak boson type, $W^\pm$ or Z^0, the interaction is referred to as charged-current (CC) or neutral-current (NC), respectively.

Hereafter water is assumed as a target material since the Super-Kamiokande water Cherenkov detector is discussed in this thesis. In the energy region from sub-GeV up to 10 GeV, neutrinos interact with nucleons inside oxygen nuclei. The dominant interaction channel for neutrino energies below ~ 1 GeV is quasi-elastic

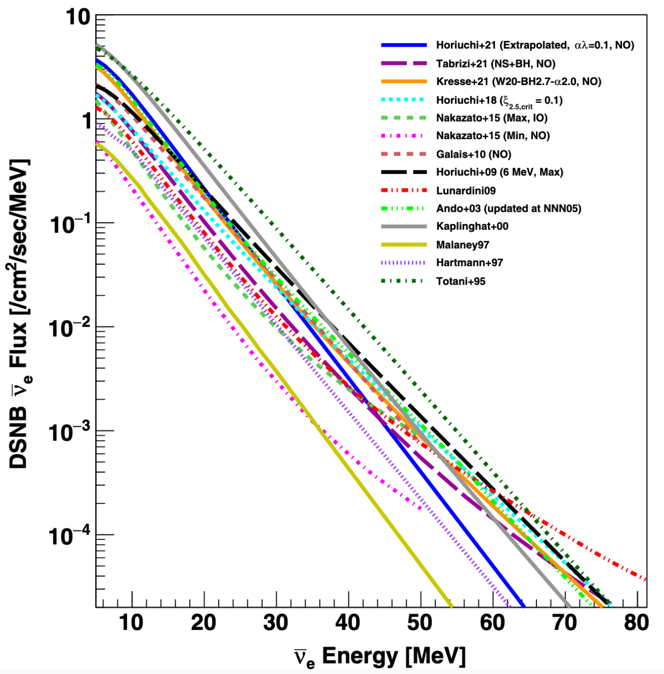

Figure 1.2: DSNB $\bar{\nu}_e$ flux predictions from various theoretical model (Horiuchi+21 [2], Tabrizi+21 [3], Kresse+21 [4], Horiuchi+18 [5], Nakazato+15 [6], Galais+10 [7], Horiuchi+09 [8], Lunardini09 [9], Ando+03 [10], Kaplinghat+00 [11], Malaney97 [12], Hartmann+97 [13], and Totani+95 [14]). This figure is taken from [15].

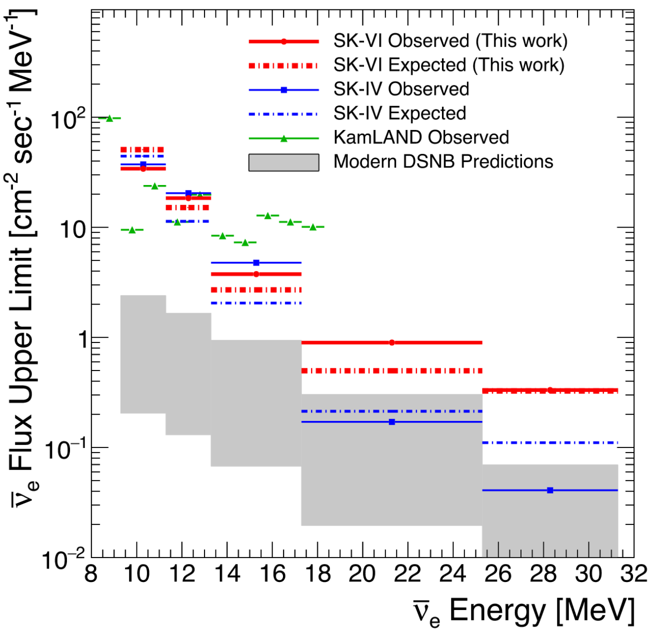

Figure 1.3: Upper limits on the $\bar{\nu}_e$ flux. The red and brue lines show the observed (solid) and expected (dotted-dashed) 90% C.L. upper limit for different period in SK. The green line represents the 90% C.L. observed upper limit placed by KamLAND [16]. The gray shaded region represents the range of the modern theoretical expectation. This figure is taken from [17].

scattering with a single nucleon. The charged-current quasi-elastic (CCQE) interaction is a quasi-elastic scattering with a single nucleon mediated by $W^{\pm}$ bosons:

$$\nu_l + {}^{16}\mathrm{O} \to l^+ + n + {}^{15}\mathrm{N}^*, \tag{1.13}$$

$$\nu_l + {}^{16}\mathrm{O} \to l^- + p + {}^{15}\mathrm{O}^*, \tag{1.14}$$

where l is the charged lepton and ν_l is the counterpart neutrino. The neutral-current quasi-elastic (NCQE) interaction is a quasi-elastic scattering with a single nucleon mediated by Z^0 bosons:

$$\nu(\bar{\nu}) + {}^{16}\mathrm{O} \to \nu(\bar{\nu}) + n + {}^{15}\mathrm{O}^*, \tag{1.15}$$

$$\nu(\bar{\nu}) + {}^{16}\mathrm{O} \to \nu(\bar{\nu}) + p + {}^{15}\mathrm{N}^*. \tag{1.16}$$

The knocked-out nucleons have a kinetic energy of a few hundred MeV. The residual nucleus is left in an excited state and undergoes de-excitation to the ground state through the emission of gamma-rays. If the excitation energy exceeds the separation energies of nucleons, the residual nucleus emits particles such as neutrons, protons and alpha particles.

In most models, the neutrino-nucleus interaction is described within the framework of the impulse approximation, where the nucleus is treated as a collection of independent nucleons, each responding to the projectile as a free particle. In this approximation, the neutrino-nucleus interaction is divided by several physical processes (Fig. 1.4).

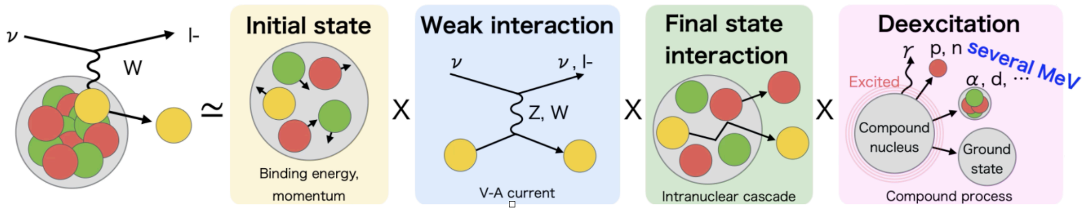

Figure 1.4: Overview of the model of the neutrino-nucleus interaction. This figure is provided by S. Abe.

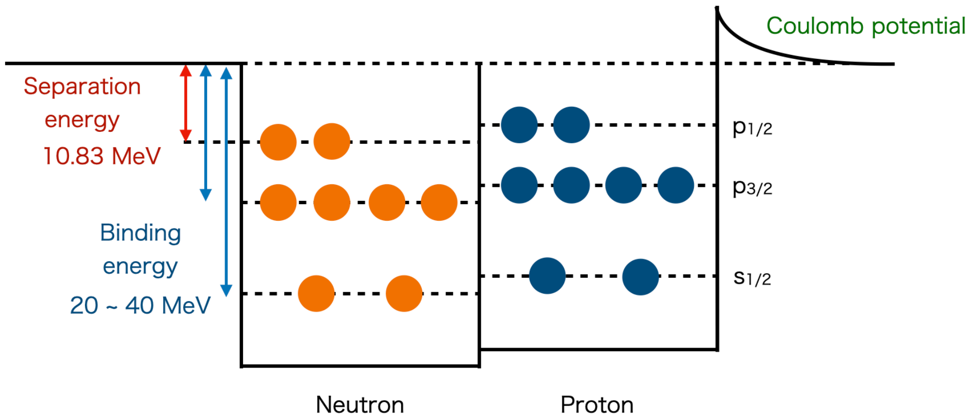

Figure 1.5: Neuclear potential of protons and neutrons for ^{16}O in the simple shell model.

Initial state

Nucleons in the nucleus are bound and have a certain momentum in the initial state. In a simple shell model, protons and neutrons in ^{16}O are in the bound state (Fig. 1.5). Two protons/neutrons are in the $s_{1/2}$ shell level, four are in the $p_{3/2}$ shell level and two are in the $p_{1/2}$ shell level for ^{16}O. The separation energy is equal to the minimum binding energy, corresponding to the binding energy of $p_{1/2}$ state.

The initial state in ^{16}O is well-understood both theoretically and experimentally, with experimental data from electron scattering experiments showing strong agreement with theoretical models [31].

Final state interaction

After one nucleon interacts with a neutrino via weak interaction, it re-scatters with other nucleons. This process is called the final state interaction (FSI). FSI is described with the cascade model. A particle propagating through the nucleus are moved by small steps and determined whether they are scattered or not at each step. This calculation is repeated until it leave the nucleus.

The FSI in ^{16}O is well-understood by nucleon scattering experiment [24, 32, 33].

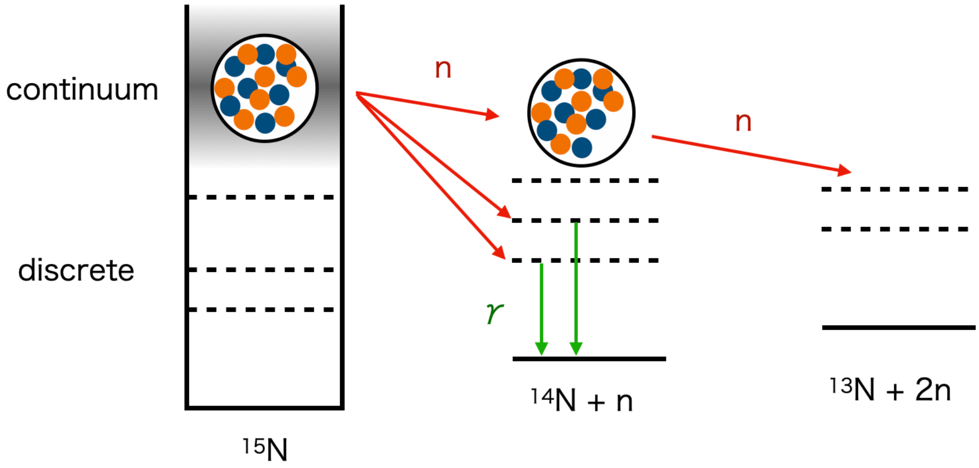

Figure 1.6: Schematic of nuclear levels and de-excitation process.

For example, the experiments [32, 33] using neutron beam and water target are carried out in Osaka University's Research Center for Nuclear Physics (RCNP). They measured knocked-out neutrons from FSI and de-excitation gamma-rays. This result is utilized for the validation of the FSI models in SK.

De-excitation

After the FSI, the nucleus is often in an excited state and then transitions to its ground state. The de-excitation process produces de-excitation gamma-rays and evaporated particles.

One of the formalisms that describes the de-excitation process is the Hauser-Feshbach model [34]. At low excitation energy, the energy levels of the nucleus are discrete. At high excitation energy, there are many levels which cannot be separated experimentally. This continuous region is described as a level density $\rho = dn/dE$. The values of level density vary with nuclei. The de-excitation process is described as a process that moves through multiple levels (Fig. 1.6). If the excitation energy is lower than the separation energies, it simply goes to the ground state with gamma-ray emissions. If the excitation energy is high, one-step de-excitation rarely leads to the ground state and the nucleus transitions to the excited state of other nuclei, resulting in the emission of evaporated particles. Then it undergoes an additional de-excitation process going to the ground state with gamma-ray emissions, or another nucleus with particle emissions. These steps are repeated until it reaches the ground state.

The nucleon scattering experiments have been utilized to understand the de-excitation process. However, since residual nuclei and most evaporation neutrons cannot be detected due to their low energy, validating the de-excitation models is difficult. The de-excitation from highly excited state result in the emission of evaporated particles, and this process is poorly understood at present.

1.3 Research Motivation

In Sec. 1.1, DSNB and its experimental status were described. The experimental data in SK are approaching the theoretical predictions. However, as will described in Sec. 2.3, the uncertainties on neutrino-nucleus interaction prediction are preventing the discovery of DSNB. These uncertainties originate from a poor understanding of the nuclear de-excitation process. To solve this problem, we plan to conduct SAMURAI-79 experiment, an inverse kinematics experiment for measuring these process. We aim to measure the branching ratios of the major channels from the de-excitation of ^{15}N, ^{15}O and ^{16}O as a function of excitation energy. In conducting this experiment, it is necessary to study the feasibility and develop appropriate measurement methods as follows:

1. Method and the precision of the measurement of excitation energy reconstruction.

2. Precision of the measurement of branching ratios.

We conducted simulation studies to investigate them. In particular, we focus on the measurement of ^{15}N in this thesis.

1.4 Statement of Originality

Chapter 4 describes the simulation used for this thesis. Basic software tools were prepared by others. I implemented event generation method with continuous distribution of excitation energy, and generated simulated sample used for the studies presented in this thesis.

Chapter 5 describes the excitation energy reconstruction. The measurement will be conducted with a newly developed detector. This work is the first study to simulate this detector in combination with other detectors. This is independently done by myself.

Chapter 6 describes the measurement of de-excitation process. The simulation of the measurement of de-excitation products from ^{15}N is done by myself.

Chapter 7 summarizes this thesis, describing an expected impact on DSNB search and future prospects. I made the estimation of the statistical performance of the measurement of branching ratio by using the result presented in Chapters 5 and 6. In addition, I calculated the expected future sensitivity of the DSNB search at SK to check the impact of this experiment on it.

Chapter 2

Search for Diffuse Supernova Neutrino Background at Super-Kamiokande

This chapter describes the Super-Kamiokande (SK) and the DSNB search at SK. At first, the overview of the SK detector is described in Sec. 2.1. The current status of the DSNB search at SK is described in Sec. 2.2. The challenges faced on the DSNB search are described in Sec. 2.3.

2.1 Overview of Super-Kamiokande

2.1.1 Super-Kamiokande Detector

SK is a water Cherenkov detector located about 1000 m under Mt. Ikeno in Kamioka, Gifu Prefecture of Japan (Fig. 2.1). The detector is a cylinderical shape with a diameter of 39.3 m and a height of 41.4 m and filled with 50 kton of gadolinium-doped pure water. It is optically separated into the inner detector (ID) and the outer detector (OD). 20-inch and 8-inch photomultiplier-tubes (PMTs) are implemented in ID and OD, respectively.

In SK, observable is the Cherenkov radiation emitted by charged particles traveling through the detector at speeds exceeding the speed of light in water. The momentum threshold for the Cherenkov radiation is 0.57 MeV/c for electrons, 118 MeV/c for muons, and 1051 MeV/c for protons.

2.1.2 SK-Gd

In pure water, neutrons are captured by hydrogen and a single 2.2 MeV gamma-ray is emitted. However, this signal is difficult to distinguish from background events due to its low energy. In order to improve the detection efficiency of the neutron, gadolinium (Gd) was dissolved in the pure water in the tank. Neutrons are captured by Gd and result in gamma-ray emissions with a total energy of ~ 8 MeV. Dissolution was started in 2020. This new experimental phase is called

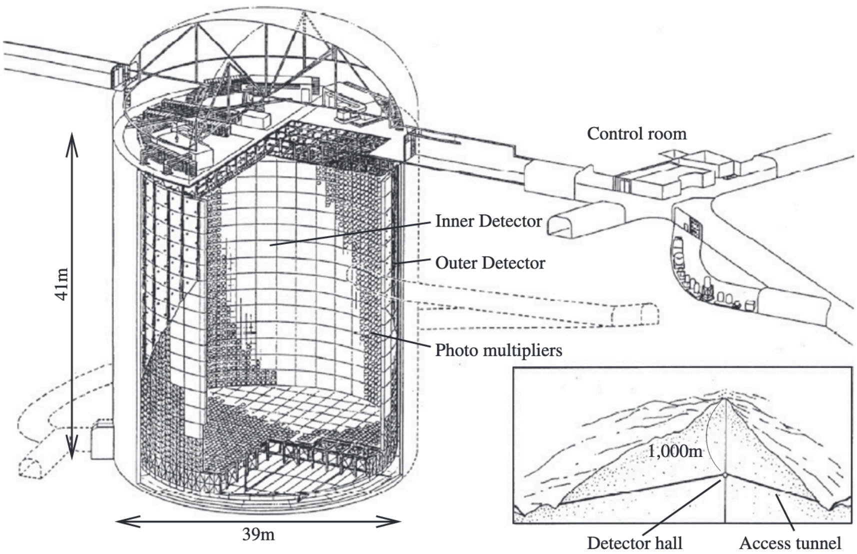

Figure 2.1: Schematic of the SK detector (cutaway view). This figure is taken from [18].

SK-Gd. Currently, the mass concentration of Gd is 0.033% and neutron capture efficiency on Gd reaches 75% [35].

2.2 DSNB search in SK-Gd

2.2.1 Latest Result

The main detection channel of DSNB is the inverse beta decay (IBD) reaction:

$$\bar{\nu}_e + p \rightarrow e^+ + n. \tag{2.1}$$

The positron from IBD produces the prompt signal. The neutron is captured by the Gd and results in multiple gamma-ray emissions (delayed signal). Prompt events with one delayed neutron signal are selected as IBD signal candidates (Fig. 2.2).

Figure 2.3 shows the reconstructed energy spectrum in the signal energy region from the latest published result of the DSNB search at SK-Gd [17]. No significant excess over the expected background in the observed events is found in this analysis. The expected event rate is only a few events per year in the entire SK detector. Therefore, a precise understanding of thier backgrounds is critical for observing DSNB. Table 2.1 shows the systematic uncertainties of the background events. The most significant backgrounds are atmospheric neutrino interaction on oxygen.

2.2.2 Atmospheric Neutrino Background

Atmospheric neutrinos are produced in the Earth's atmosphere through the decay of mesons and muons originating from cosmic rays. Their energies are from

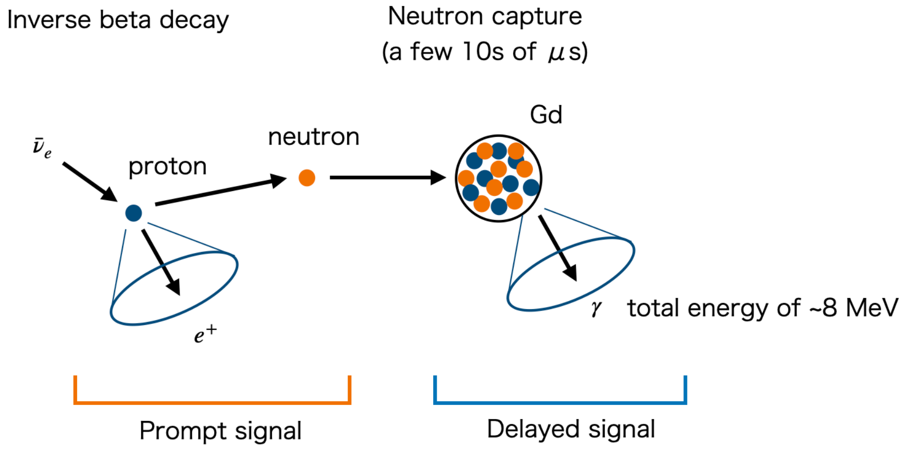

Figure 2.2: Illustration of the DSNB signal.

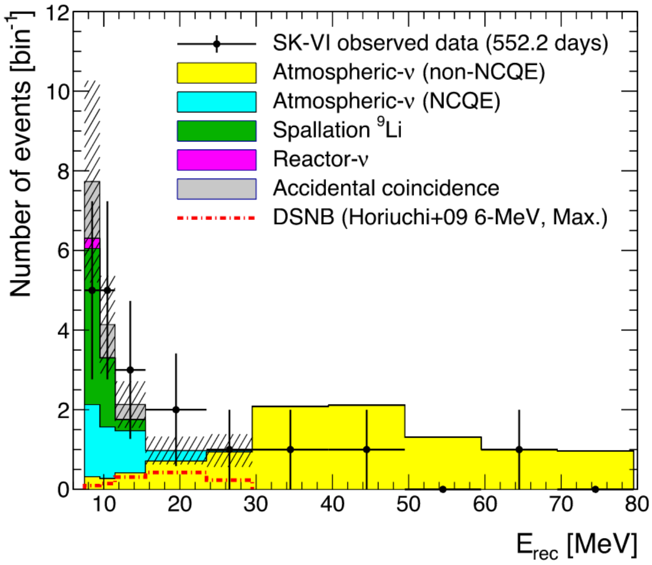

Figure 2.3: Reconstructed energy spectrum in the DSNB search at SK-Gd. Black points represent data and the error bars represent the statistical uncertainty. The colored histograms represent predicted backgrounds and hatched areas represent the total systematic uncertainty for each bin. The red dotted-dashed line shows the DSNB expectation from the Horiuchi+09 model [8]. This figure is taken from [17].

Table 2.1: Systematic uncertainties in the DSNB search at SK-Gd [21].

Backgrounds	Uncertainty
Atmospheric ν (NCQE)	68%
Atmospheric ν (Non-NCQE)	36%
Spallation ^{9}Li	55%
Reactor ν	100%
Accidental coincidence	5%

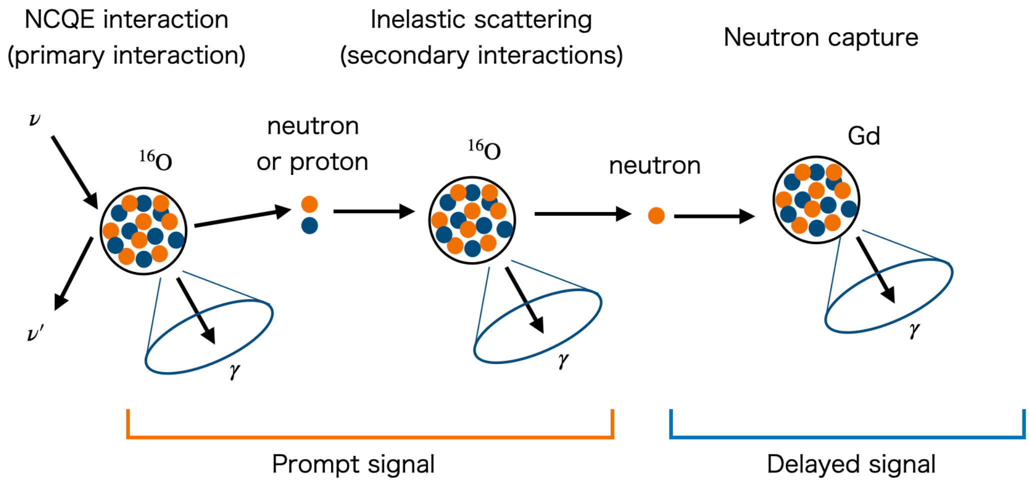

Figure 2.4: Illustration of the atmospheric neutrino NCQE background.

$\mathcal{O}(100)$ MeV to $\mathcal{O}(1)$ GeV. The events of the atmospheric neutrino NCQE and non-NCQE interaction on oxygen can produce a signal with the same topology as the DSNB signals, and mimic them.

NCQE event

Figure 2.4 shows the NCQE interaction and the following interactions. If one or more nucleons are knocked out from an oxygen nucleus by the NCQE interaction with a high-energy neutrino, the remaining nucleus is left in an excited state and undergoes de-excitation through the emission of gamma-rays or evaporated particles. This reaction is called the primary interaction. Knocked-out nucleons often inelastically interact with the other oxygen nuclei and deduce the emission of de-excitation gamma-rays and evaporated particles. These reactions are called the secondary interactions. This results in the generation of multiple gamma-rays. The sum of the gamma-rays produced by both primary and secondary reactions mimics the prompt DSNB signal.

Since the kinetic energy of knocked-out protons and evaporated protons is lower than the energy threshold for Cherenkov radiation, they are not detected in SK. All neutrons produced by both primary and secondary interaction are captured by Gd and emit gamma-rays. All neutrons regardless of their initial energy can be detected. These neutrons mimic the delayed DSNB signal.

non-NCQE event

Atmospheric neutrino backgrounds other than NCQE events are collectively called non-NCQE interactions.

The most dominant background source from non-NCQE interaction is ν_μ-CCQE interaction (Fig. 2.5). When the ν_μ-CCQE interaction produces an invisible muon, whose energy below the Cherenkov radiation threshold and decays into electrons or positrons with a lifetime of 2.2 µs, they mimic the prompt DSNB

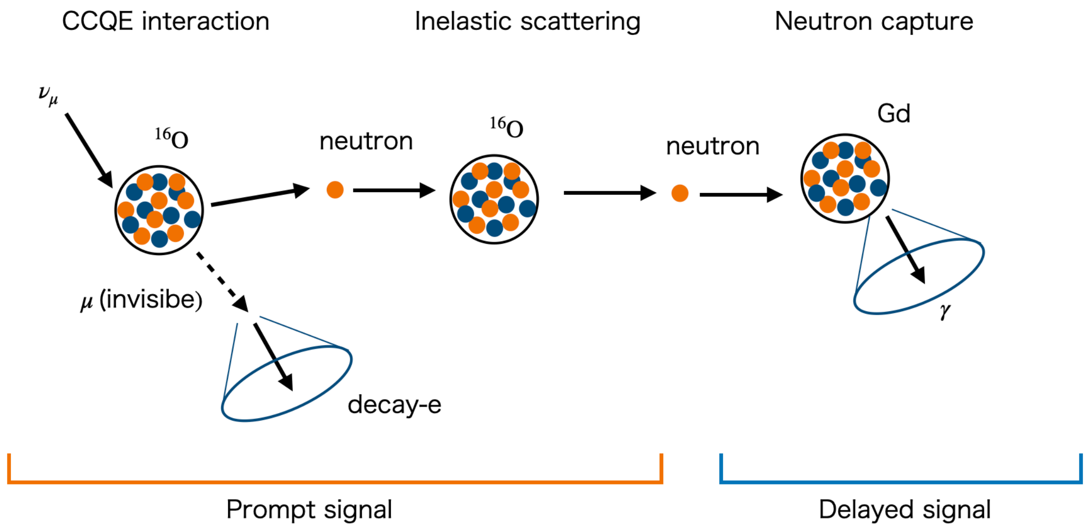

Figure 2.5: Illustration of the atmospheric neutrino ν_μ-CCQE background.

signal. The neutrons produced by both primary and secondary interaction are captured by Gd and mimic the delayed DSNB signal.

One of the subdominant background sources from non-NCQE interaction is ν_e-CCQE interaction (Fig. 2.6). In the this interaction, an electron/position is produced by the primary interaction, and multiple gamma-rays are produced by both primary and secondary interaction. This charged lepton and these gamma-rays mimic the prompt DSNB signal. All neutrons produced by both primary and secondary interaction are captured by Gd and mimic the delayed DSNB signal.

2.3 Challenges in the Background Event Prediction

2.3.1 Uncertainties on the NCQE Interaction Events

Table 2.2 shows the breakdown of the systematic uncertainties on the NCQE interaction events. The total systematic uncertainty is calculated by summing the individual uncertainties in quadrature. The main contributions are the uncertainties of NCQE cross section, neutron multiplicity, and spectral shape. These large uncertainties come from discrepancies between the data and predictions, particularly in the production of gamma-rays and neutrons from both primary and secondary interactions.

NCQE cross section

The cross section of the NCQE interaction in SK is measured by the T2K beam [22]. There are six sources of systematic uncertainty: the neutrino flux model, the neutrino interaction model, the primary-gamma and secondary-gamma emission

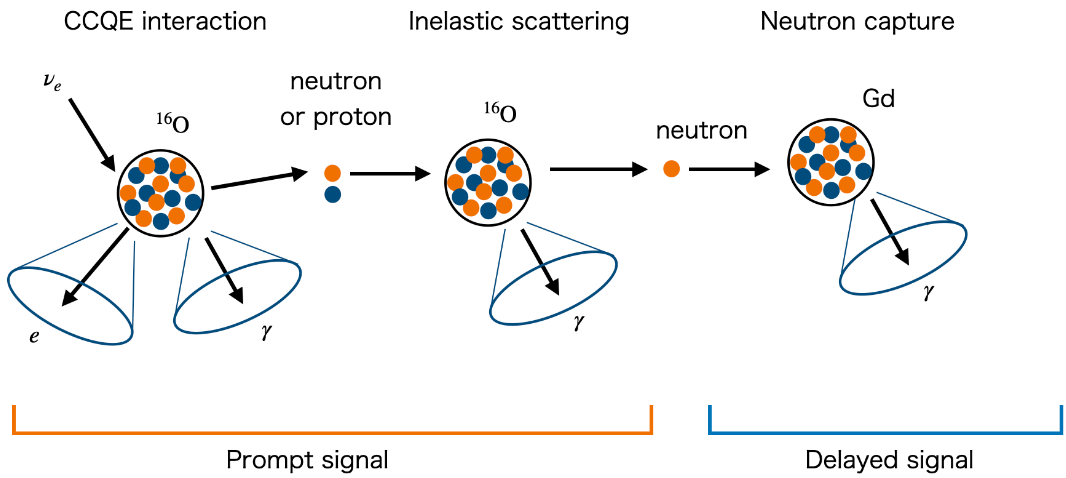

Figure 2.6: Illustration of the atmospheric neutrino ν_e-CCQE background.

Table 2.2: Summary of the systematic uncertainties on the NCQE interaction events [21].

NCQE cross section	44%
Atmospheric ν flux	15%
Flux difference	7%
Reductions	2%
Neutron tagging efficiency	9%
Neutron multiplicity	30%
Spectral shape	37%
Total	68%

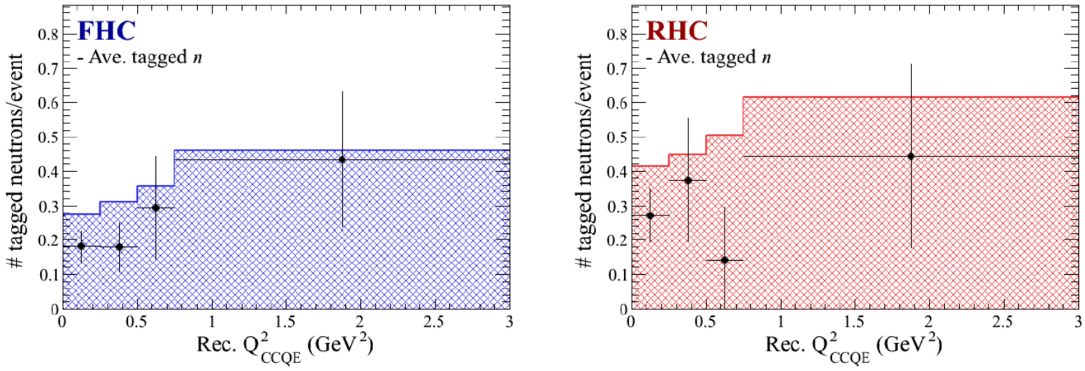

Figure 2.7: Average of the number of tagged neutrons in the T2K CC-dominant samples, as a function of reconstructed four momentum Q^2. FHC (RHC) represents the data obtained for (anti-)neutrino dominant beam. Black points represent data. The colored histograms represent prediction. These figures are taken from [19], and the original work was done by [20].

models, neutrino oscillation parameters, and the detector response. The total systematic uncertainty is calculated by summing the individual uncertainties in quadrature. The gamma-ray emission in both primary and secondary interaction is model-dependent, and this dependence is treated as a systematic uncertainty, which represents the leading source of uncertainty.

Neutron multiplicity

Multiple neutrons are produced by both primary and secondary interactions and detected regardless of their initial energy. Figure 2.7 shows the averaged tagged neutron multiplicity measured by the T2K experiment with the CC-dominant samples [20]. There are discrepancies on the data and the prediction. These discrepancies are accounted for as a systematic uncertainty of 30%.

Spectral shape

The gamma-rays produced by by both primary and secondary interactions create multiple Cherenkov rings. These are difficult to be separated and observed as a single Cherenkov ring. Figure 2.8 shows the reconstructed Cherenkov angle distribution obtained by the T2K NCQE cross section measurement [22]. In the signal region $\theta_C \in [38°, 53°]$, the data exceeded the predictions. However, the data falls short of the prediction for larger angle regions, which are dominated by multiple gamma-ray events from the NCQE interaction events. These discrepancies are accounted for as a systematic uncertainty of 37%.

2.3.2 Uncertainties on the non-NCQE Interaction Events

Table 2.3 shows the breakdown of the systematic uncertainties on the non-NCQE interaction events. The uncertainties of neutron tagging efficiency and neutron

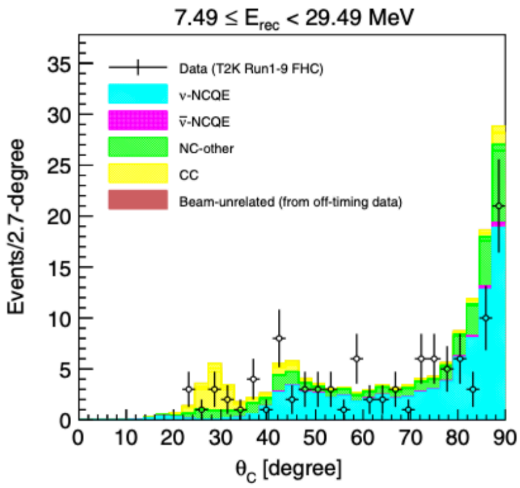

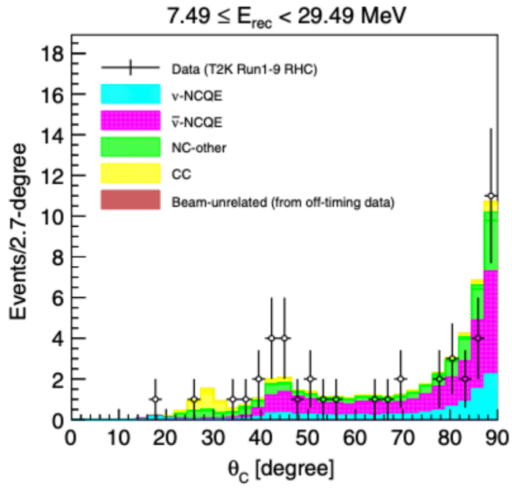

Figure 2.8: Reconstructed Cherenkov angle distribution in the T2K measurements. FHC (left) and RHC (right) are obtained for neutrino and anti-neutrino dominant beam, respectively. These figures are taken from [21], and the original figures are written in [22].

Table 2.3: Summary of the systematic uncertainties on the non-NCQE interaction events [21].

Scaling factor	17%
Neutron tagging efficiency	9%
Neutron multiplicity	30%
Total	36%

multiplicity is the same as that of NCQE. The main contribution to the total systematic uncertainty is the uncertainty on neutron multiplicity. The total systematic uncertainty is calculated by summing the individual uncertainties in quadrature.

2.3.3 De-excitation Process Following the NCQE Interaction Events

From the atmospheric neutrino NCQE interaction and the following interactions, several neutrons are produced. There are four origins of neutrons as follows:

1. Knocked-out neutrons produced by the primary interaction.

$$\text{e.g.)}\ \nu + {}^{16}\mathrm{O} \to \nu' + {}^{15}\mathrm{O}^* + n \tag{2.2}$$

2. Evaporated neutrons from the de-excitation of the nuclei produced by the primary interaction.

$$\text{e.g.)}\ {}^{15}\mathrm{N}^* \to {}^{14}\mathrm{N} + n \tag{2.3}$$

3. Knocked-out neutrons produced by the secondary interaction.

$$\text{e.g.)}\ n + {}^{16}\mathrm{O} \rightarrow {}^{15}\mathrm{O}^{*} + 2n \tag{2.4}$$

4. Evaporated neutrons from the de-excitation of the nuclei produced by the secondary interaction.

$$\text{e.g.)}\ {}^{16}\mathrm{O}^{*} \rightarrow {}^{15}\mathrm{O} + n \tag{2.5}$$

Figure 2.9 shows the simulated number of neutrons produced by the NCQE interaction as a function of the distance between the vertex of the primary interaction and that of the neutron capture. This simulation is done by SKG4, a Geant4[23]-based simulation for SK[1]. In this simulation, the reaction of the atmospheric neutrino and the detector response are simulated. The NCQE events are selected by applying the standard selection method used in SK. The primary interaction is simulated by NEUT [36]. For neutrons with energies above 20 MeV and protons, the secondary interaction is simulated using INCL [37] for the final state interaction (FSI) process and G4PreCompound (Sec. 6.1.1) for the de-excitation process. For neutrons with energies below 20 MeV, the secondary interaction is determined by ENDF database [38]. The neutrons are classified by their origins as follows:

1. Primary
   Neutrons produced by the primary interaction and captured without undergoing the secondary interactions.

2. Cascade
   Neutrons produced by the FSI in the secondary interaction and captured without undergoing another secondary interaction.

3. Casc.-origin
   Neutrons produced by the secondary interaction of the neutron whose energy is lower than 20 MeV and produced by the FSI in another secondary interaction.

4. De-excitation
   Neutrons produced by the de-excitation in the secondary interaction and captured without undergoing another secondary interaction.

5. De-Ex.-origin
   Neutrons produced by the secondary interaction of the neutron whose energy is lower than 20 MeV and produced by the de-excitation in another secondary interaction.

6. Others

The half of (1) primary neutrons, (4) de-excitation neutrons, and (5) De-Ex.-origin neutrons originate from the de-excitation. They amount to $\sim 50\%$ total detected neutrons from NCQE interaction.

[1]The simulation was performed by R. Akutsu.

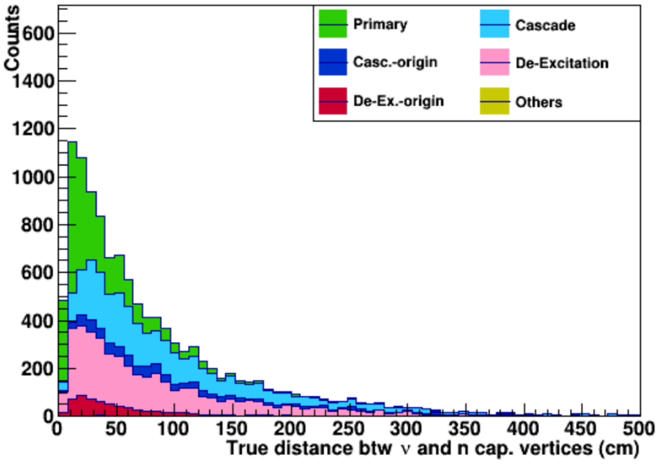

Figure 2.9: Simulated number of neutrons produced by the NCQE interaction as a function of the distance between the vertex of the primary interaction and that of the neutron capture. The simulation is done by SKG4, a Geant4[23]-based simulation for SK. The histograms are colored according to the origin of neutrons.

Table 2.4: Simulated ratio of the nuclei for all nuclei produced after the FSI in the secondary interaction. The left (right) column lists the nuclei produced by the secondary interactions with neutrons (protons).

n–^{16}O		p–^{16}O	
^{16}O*	30.6%	^{15}O*	3.0%
^{15}N*	23.6%	^{16}O*	2.7%
^{16}N*	9.3%	^{17}F*	1.3%
^{17}O*	8.3%	^{15}N*	1.3%
^{15}O*	7.7%	^{16}F*	0.7%
Others	9.9%	Others	0.9%

Table 2.4 shows the simulated ratio of the nuclei for all nuclei produced after the FSI in the secondary interaction. Three nuclei, ^{15}N*, ^{15}O* and ^{16}O* accounts for 65% of the total residual nuclei. Therefore, understanding the de-excitation process of ^{15}N*, ^{15}O* and ^{16}O* is important to improve the NCQE background prediction.

2.3.4 Measurement of De-excitation Process

The SAMURAI-79 experiment aims to measure the de-excitation process of ^{15}N*, ^{15}O* and ^{16}O*. By measuring these process and applying this result to prediction models, we can reduce the systematic uncertainties of NCQE cross section, neutron multiplicity, and spectral shape in NCQE event. Sicne these nuclei are also produced by non-NCQE events, this experiment contributes to reduce the systematic uncertainty of neutron multiplicity listed in Table 2.3. The details of this experiment are described in the next chapter.

Chapter 3

SAMURAI-79 Experiment

This chapter describes the SAMURAI-79 experiment, an inverse kinematics experiment using oxygen beam for measuring the nuclear de-excitation process of ^{15}N, ^{15}O, and ^{16}O. The basic concept of this experiment is described in Sec. 3.1. The method to improve the neutrino-nucleus interaction prediction by applying the experimental data is also described in this section. The experiment will be conducted at RIBF, RIKEN Nishina Center. The facilities of RIBF are described in Sec. 3.2. The experimental method is described in Sec. 3.3.

3.1 Concept of the SAMURAI-79 Experiment

There are large uncertainties in predicting the interaction between atmospheric neutrinos and oxygen nuclei. The key process is the de-excitation of ^{15}N*, ^{15}O* and ^{16}O* produced by the interaction between atmospheric neutrino and oxygen nuclei. Experimental data is insufficient for the de-excitation process of these nuclei.

We aim to measure the nuclear de-excitation process, especially the branching ratios as a function of excitation energy and the energy spectra of gamma-rays and neutrons. In order to understand the de-excitation process, an inverse kinematics experiment is a strong tool.

3.1.1 Inverse Kinematics

Figure 3.1 illustrates the difference between normal kinematics and inverse kinematics.

In a normal kinematics experiment, a nucleon beam is struck into a nuclear target. Recoil nucleons are detectable because their energies are sufficiently larger than the detector threshold. On the other hand, the residual nuclei are not detectable because their recoil energy is small. Similarly, most of the de-excitation products from residual nuclei are difficult to detect because their typical energies are below the detector threshold.

Figure 3.2 shows the energy spectra of the de-excitation products from ^{15}N*, ^{15}O* and ^{16}O*. The energy of most de-excitation products is below 10 MeV. Ap-

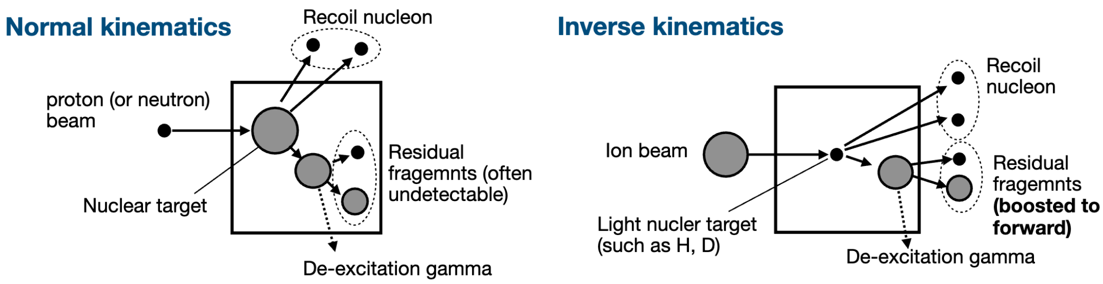

Figure 3.1: Schematic of the difference between normal kinematics and inverse kinematics. This figure is provided by Y. Nakajima.

proximately half of the neutrons have kinetic energies lower than the detector threshold imposed at the normal kinematics experiment of the $^{16}\mathrm{O}(p, 2p)^{15}\mathrm{N}$ reaction [24]. The spectrum shapes vary from model to model and this trend is also seen in the low energy region. It is important to detect these low energy nucleons for precisely predicting the particle emission.

An inverse kinematics experiment can solve the problems described above. In an inverse kinematics experiment, a nuclear beam is struck into a nucleon target. The entire system is moving relative to the lab frame. The residual nuclei and de-excitation products have high energy in the lab frame and can be detected. Consequently, an inverse kinematics experiment is suitable for measuring the de-excitation process.

3.1.2 Application of Experimental Data to Prediction Model

We plan to measure the branching ratios as a function of excitation energy. The result is utilized to tune the model parameters in the Hauser-Feshbach model. The improved model will be implemented in the nuclear reaction simulator, CCONE [39]. Then CCONE will be incorporated into the neutrino interaction simulators. We also plan to measure the energy spectra of gamma-rays and neutrons. These results will be used for validating the simulators.

3.1.3 Overview of the Experiment

We plan to conduct the SAMURAI-79 experiment for measuring the de-excitation process of $^{15}\mathrm{N}^*$, $^{15}\mathrm{O}^*$ and $^{16}\mathrm{O}^*$. This experiment will be conducted in the following four phases:

1. Measurement of the de-excitation process of $^{15}\mathrm{N}^*$ produced by the $^{16}\mathrm{O}(p, 2p)^{15}\mathrm{N}^*$ reaction at 200 MeV/u.

2. Measurement of the de-excitation process of $^{15}\mathrm{O}^*$ produced by the $^{16}\mathrm{O}(p, pn)^{15}\mathrm{O}^*$ reaction at 200 MeV/u.

3. Measurement of the de-excitation process of $^{16}\mathrm{O}^*$ produced by the $^{17}\mathrm{O}(p, pn)^{16}\mathrm{O}^*$ reaction at 200 MeV/u.

This study focuses on the first phase.

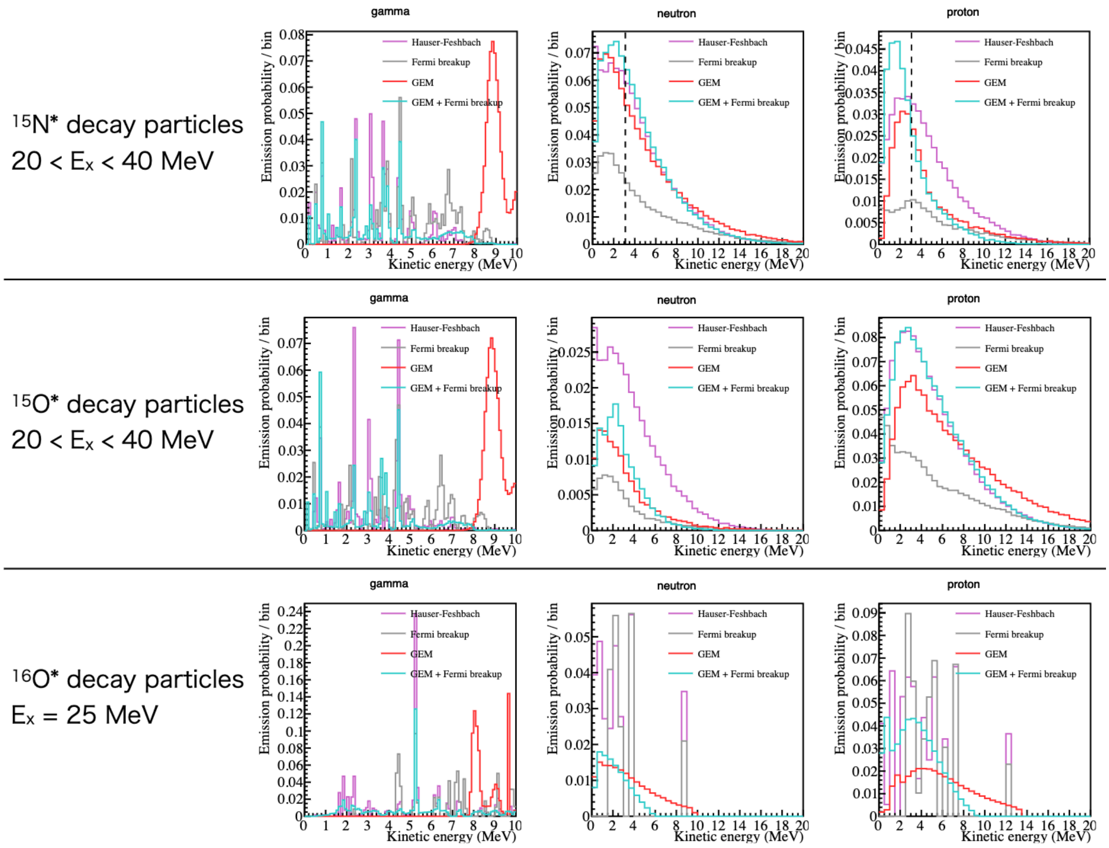

Figure 3.2: Energy spectra of gamma-rays, neutrons and protons emitted in the de-excitation process of ^{15}N, ^{15}O, ^{16}O predicted by various models. The vertical dashed lines shown in ^{15}N indicate the energy thresholds imposed at the normal kinematics measurement at RCNP [24].

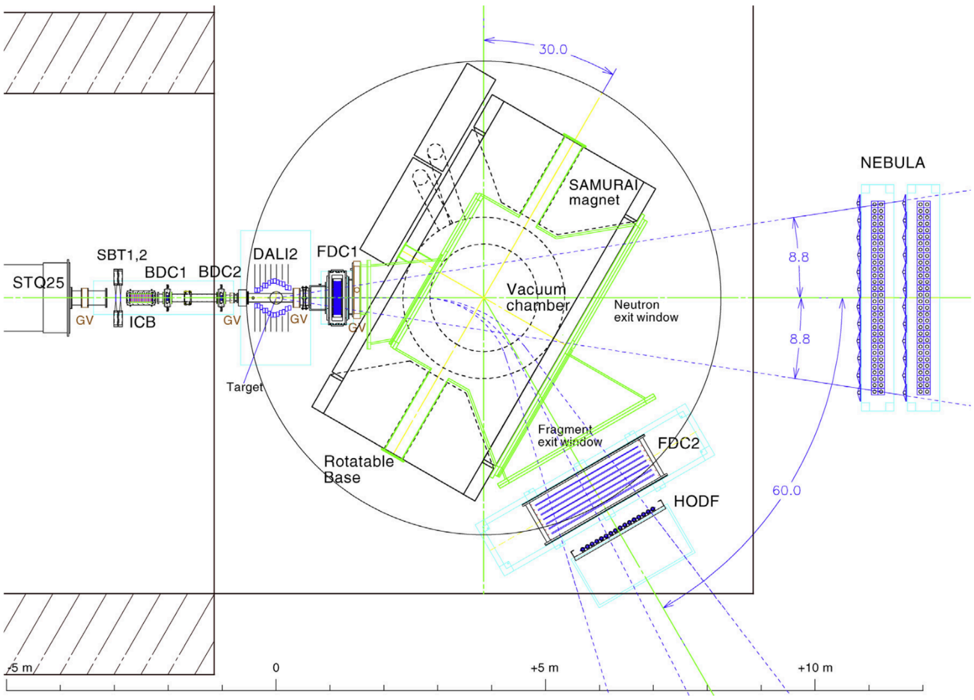

Figure 3.3: Experimental setup of the SAMURAI spectrometer. This figure is taken from [25]. This setup is as of March 2012, some detectors have been updated now.

3.2 RIBF and SAMURAI spectrometer

RI Beam Factory (RIBF) is a multistage accelerator complex located at RIKEN Nishina Center. It can generate $20-300\,\mathrm{MeV/u}$ radioactive isotope beam. The fragment separator BigRIPS is used to produce and purify the secondary beam from the primary RI beam. On one of the ends of the BigRIPS beam line, there are a large superconductive magnet and a variety of detectors called SAMURAI spectrometer [25]. SAMURAI stands for Superconducting Analyser for MUlti particles from RAdio Isotope Beams. Various nuclear physics experiments have been conducted there.

The SAMURAI spectrometer (Fig. 3.3) is designed to detect all particles produced by the reaction for kinematically complete experiments. It is composed of a magnet, beam detectors, charged particle detectors, neutron detectors, and gamma-ray detectors. The details of these equipment are described below.

SBT1, SBT2

SBT1 and SBT2 are plastic scintillators with two PMTs on both sides. They are placed in front of the target. They measure the passing time of the beam and generate the beam trigger.

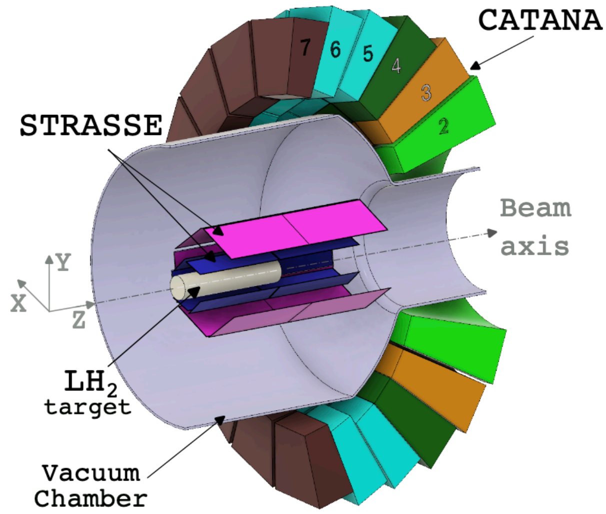

Figure 3.4: Schematic of STRASSE (inner barrel (blue), outer barrel (pink)) and CATANA. LH_2 target (gray) is 150 mm thick. This figure is taken from [26].

BDC1, BDC2

BDC1 and BDC2 are drift chambers placed just before the target. They monitor the incident positions and angles of the beam upon the target.

STRASSE

STRASSE (Silicon Tracker for RAdioactive nuclei Studied at SAMURAI Experiments) [26] is a charged-particle silicon tracker for quasi-free scattering measurement (Fig. 3.4). STRASSE consists of two layers. For each layer, detector segments are configured in a hexagonal shape. Each detector segment consists of Si wafers and their frame (Fig. 3.5).

CATANA

CATANA (CAesium iodide array for gamma-ray Transitions in Atomic Nuclei at high isospin Asymmetry) [40] is a calorimeter consisting of 140 square frustum-shaped CsI(Na) crystals coupled to PMTs. The crystals are wrapped by Teflon and encapsulated in a 0.5 mm-thick Al housing. The crystals are arranged hemispherically around the target and STRASSE (Fig. 3.4).

SAMURAI magnet

SAMURAI magnet is a superconducting dipole magnet with a maximum field of 3.1 T. This is used to identification and momentum measurement of charged particles by bending them in a magnetic field.

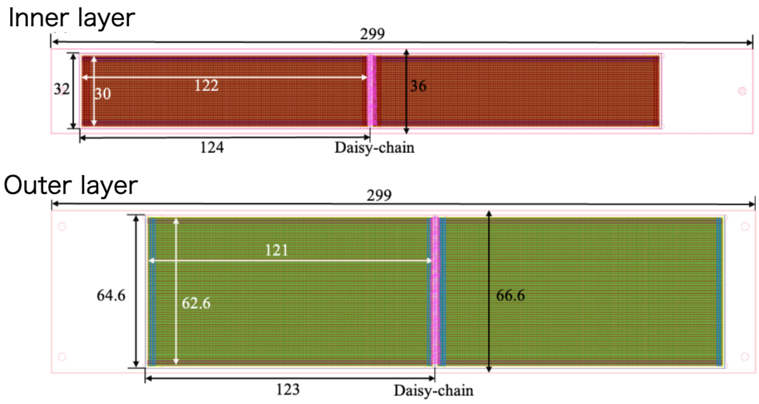

Figure 3.5: Schematic of the inner and outer silicon sensors and their frames of STRASSE. This figure is taken from [26].

NEBULA

NEBULA (Neutron-detection system for Breakup of Unstable-Nuclei with Large Acceptance) is a neutron detector array consisting of 120 plastic scintillators, arranged in two walls.

FCC1, FDC2

FDC1 and FDC2 are drift chambers. FDC1 is placed between the target and the SAMURAI magnet. FDC2 is placed after the SAMURAI magnet. They measure the track of charged particles.

HODF24

HODF24 is a charged particle detector array consisting of 24 plastic scintillators placed after the FDC2. It measures the TOF and the energy deposition of charge particles.

3.3 Experimental Method of the SAMURAI-79 Experiment

We plan to measure the de-excitation process of ^{15}N, ^{15}O and ^{16}O. This thesis focus on the measurement of the de-excitation process of ^{15}N. Figure 3.6 shows the schematic of the detector configuration for this measurement. This measurement is composed of three parts as follows (Fig. 3.7):

1. ^{16}O beam at 200 MeV/u is bombard to the LH$_2$ target and $^{16}\mathrm{O}(p, 2p)^{15}\mathrm{N}$ reaction happens.

2. The excitation energy of ^{15}N is reconstructed by measuring two recoil protons.

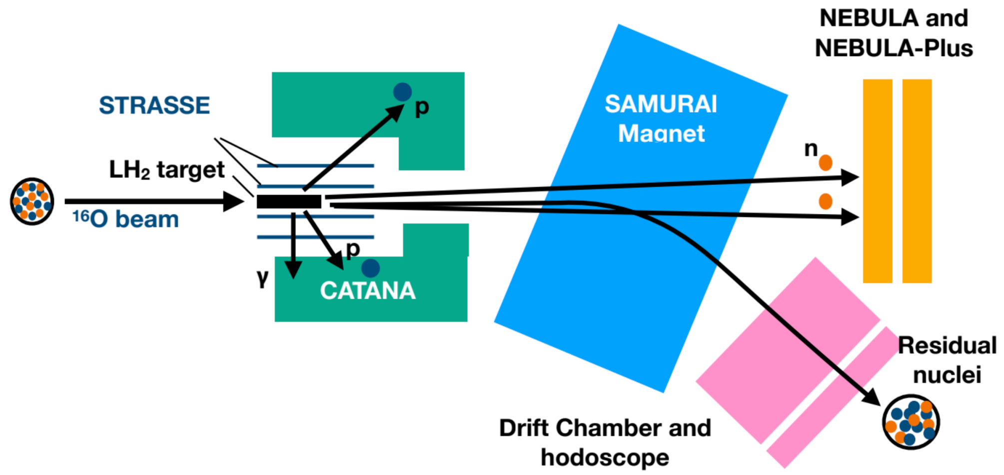

Figure 3.6: Schematic of the detector configuration for the measurement of the de-excitation process of ^{15}N. This figure is provided by Y. Nakajima.

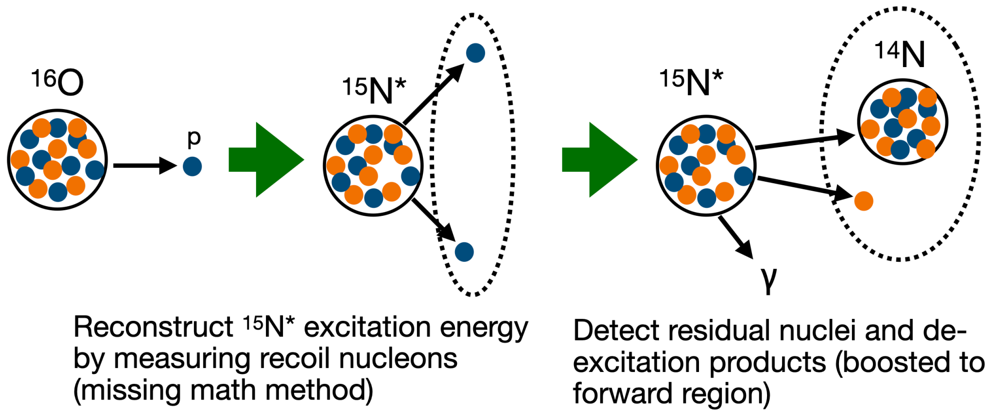

Figure 3.7: The measurement of the de-excitation process of ^{15}N. This figure is provided by Y. Nakajima.

3. The de-excitation products from ^{15}N (gamma-rays, residual nuclei, neutrons) are measured.

A beam energy of 200 MeV/u is selected because it provides a relatively clean measurement of the quasi-free $(p, 2p)$ process.

3.3.1 Primary and Secondary Beam

A primary beam of ^{18}O at 230 MeV/u is produced by RIBF accelerator. A secondary beam of ^{16}O at 200 MeV/u is produced by the projectile fragmentation of the primary beam on a 1 mm thick ^{9}Be target. The secondary beam is purified by the fragment separator BigRIPS. SBTs are used for timing and triggering. BDCs are used to measure the incident positions and angles of the beam upon the target.

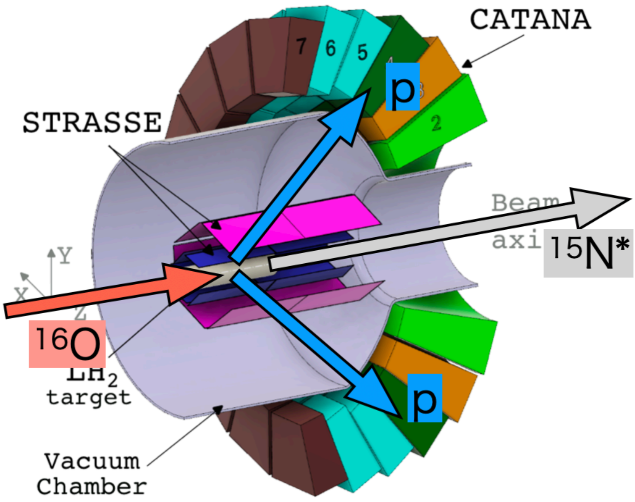

Figure 3.8: The measurement of the four momenta of two recoil protons. The excitation energy of ^{15}N is calculated by missing mass method.

3.3.2 Excitation Energy Reconstruction by Missing Mass Method

The excitation energy of ^{15}N is measured by missing mass method (Fig. 3.8). Due to energy and momentum conservation, the four momentum of ^{15}N can be calculated from the four momenta of ^{16}O and two recoil protons. The excitation energy is then calculated using the following formula:

$$E_{\mathrm{x}} = \sqrt{(E_{\mathrm{beam}} + E_{\mathrm{tgt}} - E_1 - E_2)^2 - (\vec{P}_{\mathrm{beam}} - \vec{P}_1 - \vec{P}_2)^2} - M_{\mathrm{frag}} \tag{3.1}$$

where E_{beam}, E_{tgt}, E_1, E_2 are the total energy of the beam, target and two recoil protons, respectively. $\vec{P}_{\mathrm{beam}}$, $\vec{P}_1$, $\vec{P}_2$ are the momentum of the incident beam and two recoil protons in the laboratory frame.

The four momenta of two recoil protons are measured by STRASSE and CATANA surrounding the target. The energy of the ^{16}O can be monitored by BigRIPS. Consequently, the excitation energy of ^{15}N* can be reconstructed.

3.3.3 Measurement of De-excitation Process

Particle identification of the residual nuclei

The SAMURAI magnet and the charged particle detectors are used to identify the residual nuclei. The velocity of the residual nucleus β is calculated from the TOF between HODF24 and SBTs. The atomic number of the residual nucleus Z is calculated from the β and the light yield in HODF24. The mass number of the residual nucleus A is calculated using the following formula:

$$\frac{A}{Z} = \frac{eB\rho}{m_N \beta\gamma} \tag{3.2}$$

where m_N is the atomic mass unit, e is the elementary charge and $B\rho$ is the magnetic rigidity measured by FDCs.

A charge resolution of $\sigma_Z \approx 0.16$ has been measured for RI beams up to $Z = 8$ [25]. A separation of more than 10σ was achieved for the mass number in the ^{26}O experiment [41].

Detection of the evaporated neutron

The evaporated neutrons are emitted isotropically with a typical energy below 10 MeV in the rest frame of ^{15}N. In the lab frame, They are boosted in the beam direction and detected by the plastic scintillator array NEBULA. The energy of neutrons is measured from TOF between the target and NEBULA.

A detection efficiency of $32.5 \pm 0.3(\mathrm{stat}) \pm 0.9(\mathrm{syst})\%$ for a single neutron and an energy resolution of $\sigma = 2.72$ MeV is obtained by a measurement with neutrons produced by the ^{7}Li$(p,n)^7$Be(g.s. + 0.43 MeV) reaction using a 200 MeV proton beam [42].

Detection of the de-excitation gamma-ray

The de-excitation gamma-rays are detected by the CsI calorimeter CATANA. The typical energy resolution and photo-peak efficiency for 662 keV gamma-ray are 10% (FWHM) and 14%, respectively [40].

Chapter 4

Detector Simulation

This chapter describes Monte-Carlo simulation of the SAMURAI-79 experiment. The simulation setup is described in Sec. 4.1. The method of the event generation is described in Sec. 4.2.

4.1 Simulation Setup

A simulation combining smsimulator5.5 [43] and nptool v3 [44] based on Geant4 [23] (10.7.4) is used in this study. The detectors and materials in SAMURAI are reproduced in the simulation as shown in Fig. 4.1. The beam direction corresponds to the z-axis.

STRASSE

Si wafers and PCB frames are placed in the simulation (Fig. 4.2). If a particle deposit energy in a wafer, the transeverse and longitudinal strips closest to the passing point are selected. The intersection of the two strips is recorded as an observable passing point in the simulation.

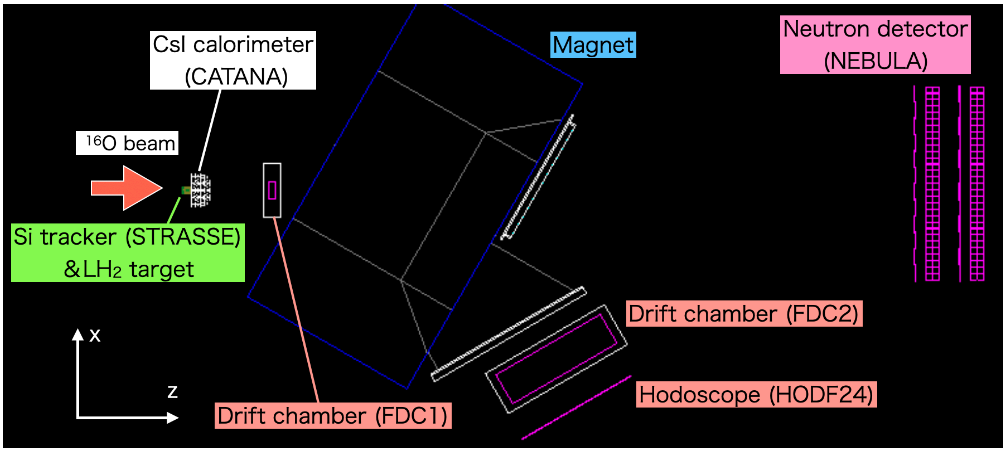

Figure 4.1: Simulation setup.

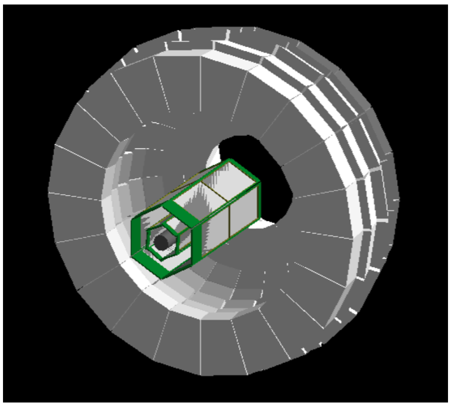

Figure 4.2: STASSE and CATANA in the simulation. LH_2 target (gray) is placed at the center. Si wafers (gray) and PCB frames (green) are placed around the target. CATANA crystals (white) are hemispherically surrounding the target and STRASSE.

CATANA

The energy deposits of the particles are summed in each crystal. The observable energy is simulated by smearing the true energy deposition E by a Gaussian with energy-dependent σ:

$$\sigma\,[\mathrm{keV}] = 0.686569 \times (E\,[\mathrm{keV}])^{0.564352}. \tag{4.1}$$

These parameters are obtained by gamma-ray source calibration.

SAMURAI magnet

The magnetic field at each position is obtained from [45]. Figure 4.3 shows the simulated distribution of the magnetic field along the z-axis. $z = 0$ corresponds to the center of the magnet.

NEBULA

When a charged particle deposits energy, the light yield is calculated depending on the type of particle (e.g., e^-, p, ^{12}C) using the following formula:

$$(\text{Light yield}) = a_1 E - a_2(1 - \exp(-a_3 E^{a_4})), \tag{4.2}$$

where E is the true energy deposition. The values of parameters $a_n\,(n = 1, 2, 3, 4)$ are listed in [27]. Figure 4.4 shows the simulated light yield as a function of energy deposition for different types of charged particles.

4.2 Event Generation

Two types of events are generated. One is generated with a fixed excitation energy of ^{15}N, the other with a continuous excitation energy distribution based on a spectral function.

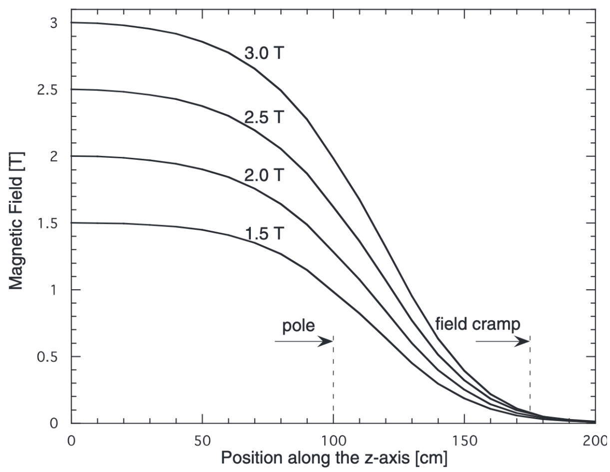

Figure 4.3: Simulated distribution of the magnetic field along the z-axis. The arrows indicate the end position of the pole and the field cramp. This figure is taken from [25].

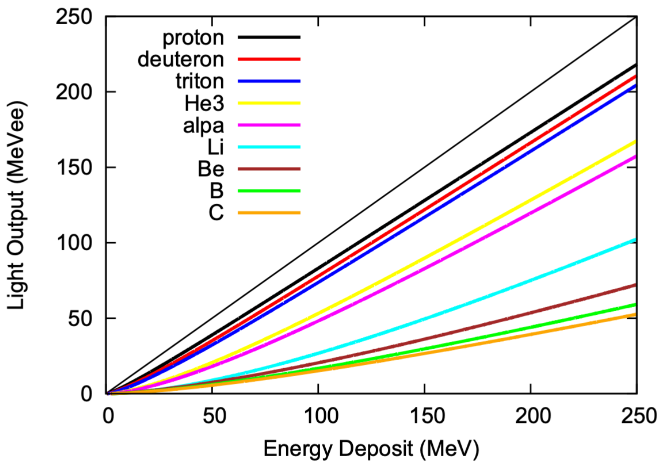

Figure 4.4: Simulated light yield as a function of energy deposition for different types of charged particles. This figure is taken from [27].

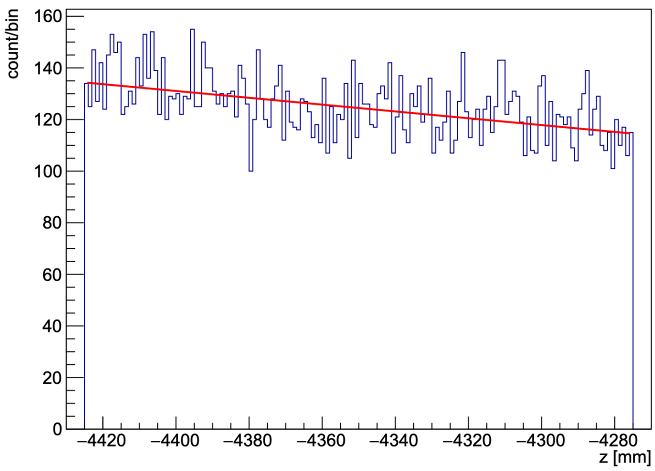

Figure 4.5: Vertex distribution. The red line represents the fitting result with a liniar function.

4.2.1 Event Generation with Fixed Excitation Energy

In the event generation, the transportation of the beam is simulated by Geant4. When the beam reaches a pre-determined vertex point, the kinematics of the $(p, 2p)$ reaction is calculated based on the kinetic energy of the beam.

Beam condition

The initial kinetic energy of the oxygen beam is 200 MeV/u and the momentum direction is parallel to the z-axis. The initial x and y coordinates are randomly distributed with a Gaussian distribution of $\sigma = 5$ mm. The center of the beam distribution is the center of the target.

Vertex position

Reactions are more likely to occur upstream of the target than downstream. To reproduce this trend, another MC sample is generated. A 200 MeV/u oxygen beam is shot into the LH_2 target. Fig. 4.5 shows the distribution of the vertex of inelastic interactions including other reactions besides the $(p, 2p)$ reaction. This distribution is fitted with a liniar function. The position of the vertex in the event generation is determined to follow this liniar distribution.

Quasi-free scattering

The reaction is treated as a quasi-free scattering in which a nucleon is removed from the nucleus by the interaction with a target nucleon. This reaction is divided into two steps as follows (Fig. 4.6):

$$\text{Virtual dissociation: } {}^{16}\text{O} \rightarrow {}^{15}\text{N} + p_{\text{virtual}}, \tag{4.3}$$

$$\text{Scattering: } p_{\text{virtual}} + p_{\text{target}} \rightarrow p + p. \tag{4.4}$$

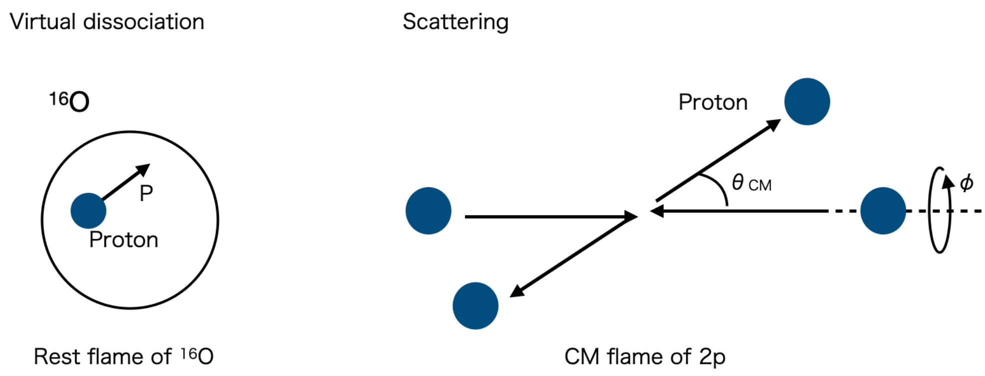

Figure 4.6: The quasi-free scattering.

The first step is dissociation. ^{16}O is dissociated into the fragment (^{15}N) and the intermediate virtual proton (p_{virtual}) with an off-shell mass $m_{p,\mathrm{off}}$. This off-shell mass is deduced from energy conservation in the rest frame of ^{16}O as follows:

$$m_{^{16}\mathrm{O}} = \sqrt{\vec{P}^2 + (m_{^{15}\mathrm{N}} + E_{\mathrm{x}})^2} + \sqrt{\vec{P}^2 + m_{p,\mathrm{off}}^2}, \tag{4.5}$$

where $m_{^{16}\mathrm{O}}$ and $m_{^{15}\mathrm{N}}$ are the masses of ^{16}O and ^{15}N, respectively. E_{x} represents the excitation energy of ^{15}N. $\vec{P}$ represents the internal momentum, the momentum of the intermediate virtual proton in the reat frame of ^{16}O. Therefore, the momentum of ^{15}N is given by $-\vec{P}$.

The simulated excitation energies are 10, 30, and 50 MeV. Each component of the internal momentum $\vec{P} = (P_x, P_y, P_z)$ is determined independently by the Gaussian distribution of $\sigma = 50$ MeV. If the momentum direction is opposite to the beam direction, the invariant mass will be insufficient to emit two protons. In this case, the internal momentum is generated again.

The second step is scattering. This is the elastic scattering between the intermediate virtual proton and the target proton. The invariant mass S of this scattering process is calculated using

$$S^2 = \left(\sqrt{\vec{P}_{\mathrm{lab}}^2 + m_{p,\mathrm{off}}^2} + m_p\right)^2 - \vec{P}_{\mathrm{lab}}^2, \tag{4.6}$$

where $\vec{P}_{\mathrm{lab}}$ is the momentum of the intermediate virtual proton in the lab frame and m_p is the physical mass of the proton. The kinematics of the two recoil protons is calculated in the center-of-mass frame assuming an isotropic scattering process. The scattering angle θ_{CM} is determined randomly so that $\cos\theta_{\mathrm{CM}}$ is uniform at $-1 \leq \cos\theta_{\mathrm{CM}} \leq 1$. The scattering angle ϕ is determined randomly to be uniform for $0° \leq \phi \leq 360°$.

De-excitation

The de-excitation of ^{15}N is calculated by G4PreCompound, the de-excitation module provided by Geant4.

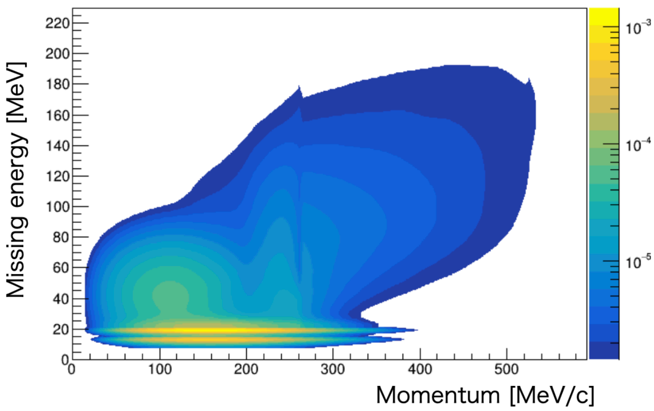

Figure 4.7: Spectral function of oxygen provided by Benhar *et al.* [28].

4.2.2 Event Generation Based on Benhar's Spectral Function

The generation method with continuous excitation energy distribution is the same as the generation with fixed excitation energy, except for the method of determining the excitation energy and the internal momentum. These values are determined based on a spectral function.

A spectral function provides a two-dimensional probability density function of nucleons as a function of missing energy and momentum, $P(p, E_{\mathrm{miss}})$. Fig. 4.7 shows the probability density function of the spectral function provided by Benhar *et al.* [28]. This spectral function is formulated by using electron scattering data. The bin resolution is increased by interporation. Missing energy and momentum magnitude are randomly determined from this distribution. A excitation energy is given by

$$E_{\mathrm{x}} = E_{\mathrm{miss}} - S_p, \tag{4.7}$$

where S_p is the separation energy of proton at ^{16}O. The direction of internal momentum is determined isotropically. The distribution of the excitation energy generated by this method is shown in Fig. 4.8. The peak at 0 MeV (8 MeV) is formed when a nucleon at the $p_{1/2}$ ($p_{3/2}$) shell level is knocked out.

4.2.3 Energy and Angular Distributions of the Generated Events

The simulated energy and angular distributions of the two recoil protons in the lab frame are shown in Figs. 4.9 to 4.12. The polar angle is defined as the angle with respect to the beam axis. The azimuthal angle relative to the beam axis is defined such that $\phi = 0°$ corresponds to the upward direction in Fig. 4.1. There are two factors contributing to the spread of these correlations: the internal momentum of the proton in the nucleus and the energy loss of the beam in the target.

Fig. 4.9 shows the kinetic energy distributions of the two recoil protons. If the reaction is pure proton elastic scattering, the sum of the kinematics energies

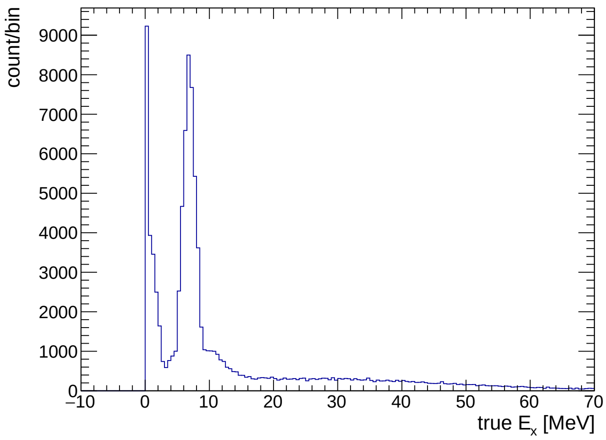

Figure 4.8: Excitation energy distribution generated based on Benhar's spectral function.

is 200 MeV due to the energy conservation. The energies become lower because of the binding energy in ^{16}O and the excitation energy of ^{15}N. The higher the excitation energy, the smaller the sum of kinetic energies tends to be.

Fig. 4.10 shows the angular distributions of the polar angles of the two recoil protons. The polar angles of the two protons decrease as the excitation energy increases. Fig. 4.10 shows the angular distributions of the azimuthal angles of the two recoil protons. At the center-of-mass flame, the two recoil protons are shot back to back. In the lab flame, two protons are boosted in the beam direction and have a back-to-back correlation in the azimuthal direction.

Fig. 4.12 shows the correlations between the polar angle and the kinetic energy of the proton. There is a correlation between the polar angle and the kinetic energy: as the kinetic energy increases, the polar angle becomes shallower.

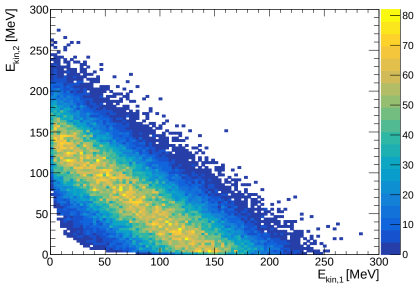

(a) $E_{\mathrm{x}} = 10\,\mathrm{MeV}$

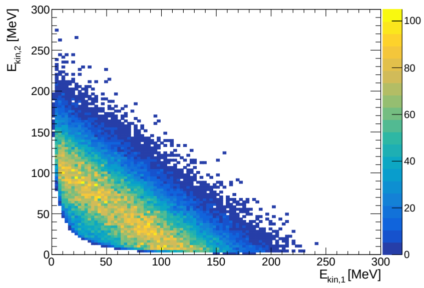

(b) $E_{\mathrm{x}} = 30\,\mathrm{MeV}$

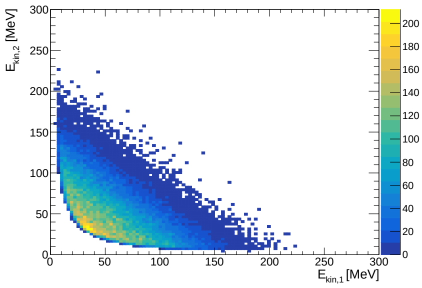

(c) $E_{\mathrm{x}} = 50\,\mathrm{MeV}$

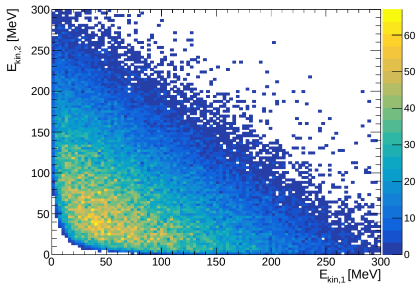

(d) Based on SF

Figure 4.9: Simulated distributions of the kinetic energies of the two recoil protons from the $^{16}\mathrm{O}(p, 2p)^{15}\mathrm{N}$ reaction with a 200 MeV/u $^{16}\mathrm{O}$ beam. All values are expressed in the lab frame.

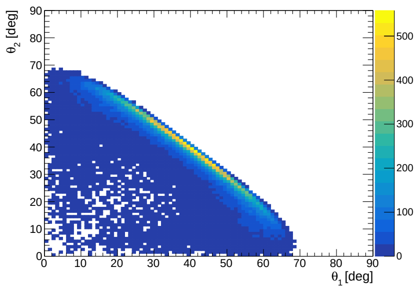

(a) $E_{\mathrm{x}} = 10\,\mathrm{MeV}$

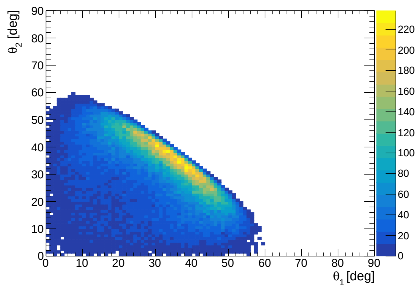

(b) $E_{\mathrm{x}} = 30\,\mathrm{MeV}$

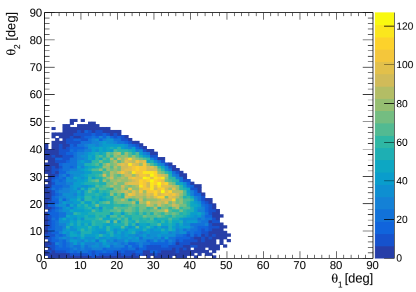

(c) $E_{\mathrm{x}} = 50\,\mathrm{MeV}$

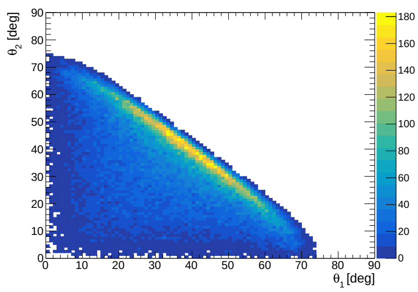

(d) Based on SF

Figure 4.10: Simulated angular distributions of the polar angles of the two recoil protons from the $^{16}\mathrm{O}(p, 2p)^{15}\mathrm{N}$ reaction with a 200 MeV/u $^{16}\mathrm{O}$ beam. All values are expressed in the lab frame.

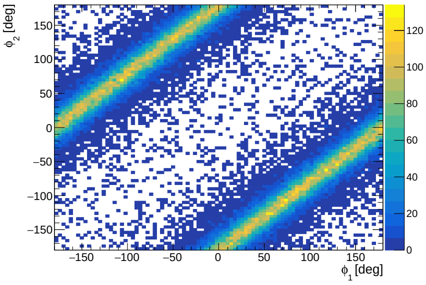

(a) $E_{\mathrm{x}} = 10\,\mathrm{MeV}$

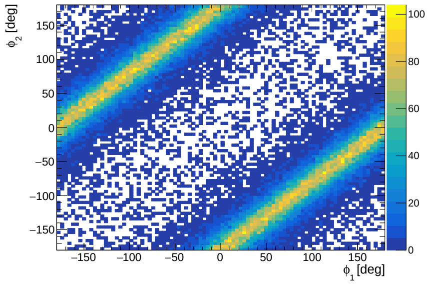

(b) $E_{\mathrm{x}} = 30\,\mathrm{MeV}$

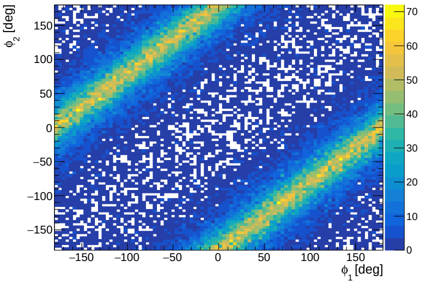

(c) $E_{\mathrm{x}} = 50\,\mathrm{MeV}$

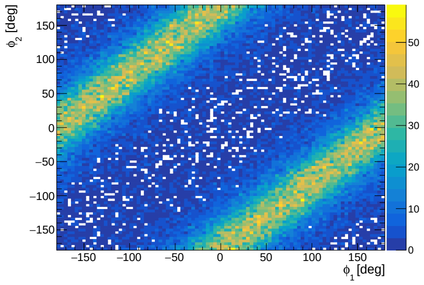

(d) Based on SF

Figure 4.11: Simulated angular distributions of the azimuthal angles of the two recoil protons from the $^{16}\mathrm{O}(p, 2p)^{15}\mathrm{N}$ reaction with a 200 MeV/u $^{16}\mathrm{O}$ beam. All values are expressed in the lab frame.

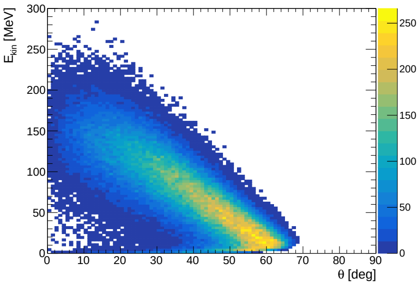

(a) $E_{\mathrm{x}} = 10\,\mathrm{MeV}$

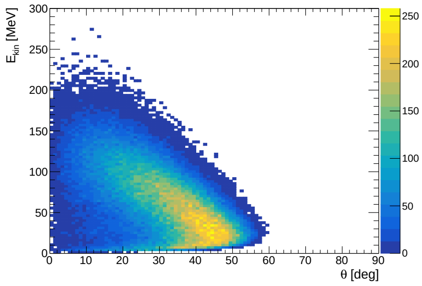

(b) $E_{\mathrm{x}} = 30\,\mathrm{MeV}$

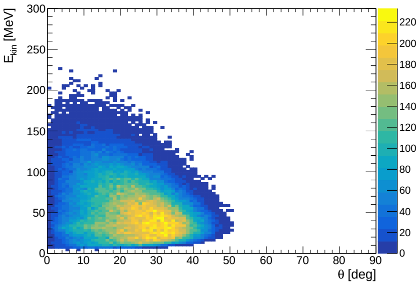

(c) $E_{\mathrm{x}} = 50\,\mathrm{MeV}$

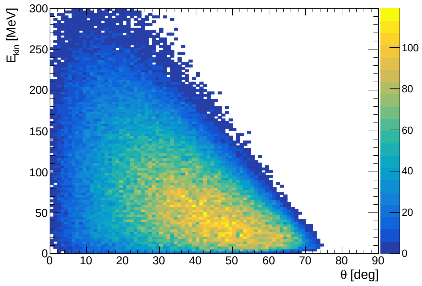

(d) Based on SF

Figure 4.12: Simulated correlations between the polar angle and the kinetic energy of the proton from the $^{16}\mathrm{O}(p, 2p)^{15}\mathrm{N}$ reaction with a 200 MeV/u $^{16}\mathrm{O}$ beam. All values are expressed in the lab frame.

Chapter 5

Excitation Energy Reconstruction

In this chapter, the method and result for reconstructing excitation energy of ^{15}N produced by ^{16}O$(p, 2p)^{15}$N reaction are described. The excitation energy of ^{15}N is reconstructed by the missing mass method. In this method, the excitation energy is determined by calculating the four momentum of ^{15}N from the four momenta of ^{16}O and two recoil protons.

The method to measure the four momenta of two recoil protons is described in Sec. 5.1. The criteria to select two recoil proton events are described in Sec. 5.2. Energy losses of oxygen beam and recoil protons are estimated in 5.3 and 5.4. The results of excitation energy reconstruction with fixed excitation energy are shown in Sec. 5.5. Factors that affect the resolution of the excitation energy is discussed in Sec. 5.6. The excitation energy reconstruction for the continuous input distribution is describe in Sec. 5.7.

5.1 Measurement of Recoil Protons

This section describes the measurement of two recoil protons produced by ^{16}O$(p, 2p)$ ^{15}N reaction. In the simulation, ^{16}O$(p, 2p)^{15}$N reactions at 200 MeV/u are generated with the fixed excitation energy of ^{15}N (described in Sec. 4.2). The excitation energies are set to 10, 30, and 50 MeV. Two recoil protons are shot and detector response is simulated (Fig. 5.1). Athough other particles such as de-excitation gamma-rays or evaporated nucleons are produced by the reaction, only two protons

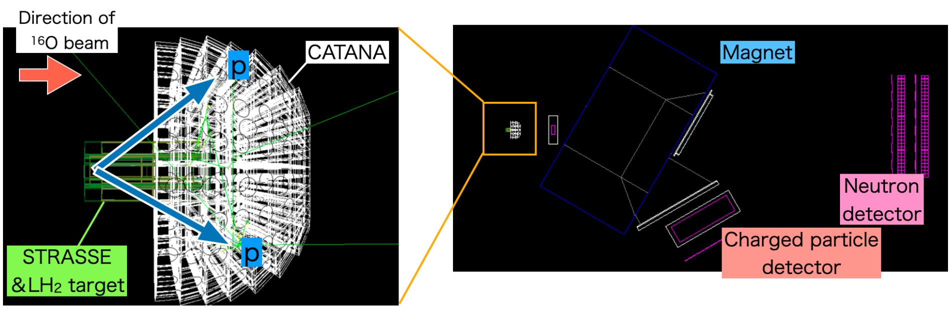

Figure 5.1: Illustration of the simulation of excitation energy reconstruction.

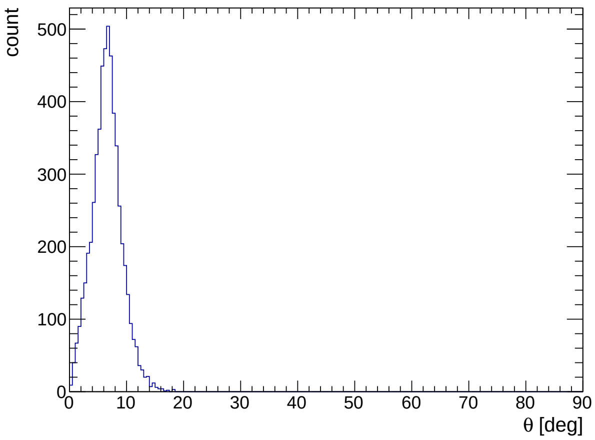

Figure 5.2: Simulated distribution of the polar angle of the evaporated protons in the lab frame.

are considered in this simulation.

STRASSE and CATANA are used to measure the momentum direction and the kinetic energy of the recoil protons.

Momentum direction

When a charged particle pass through the both of the two STRASSE layers, its track and momentum direction can be determined.

Only recoil protons, which have large scattering angle, can be observed by STRASSE. The evaporated protons are boosted in the beam direction and their polar angles are below 10° (Fig. 5.2). Therefore they do not pass through the STRASSE layers, which cover $20^\circ \lesssim \theta \lesssim 90^\circ$. The mass attenuation coefficient for 1 MeV gamma-rays in Si is $6.361 \times 10^{-2}\,\mathrm{cm^2/g}$[46], corresponding to a mean free path of 6.7 cm. As a result, 99.3% of the incident gamma-rays are not detected by the STRASSE layers with a total thickness of 0.5 mm.

Kinetic energy

Protons lose energy via ionization loss in the CATANA crystals. The mass range for 100 MeV protons in CsI is $14\,\mathrm{g/cm^2}$[29], corresponding to a range of 3 cm. Therefore, protons typically stop in a single crystal, with a thickness of ~ 10 cm. The sum of energy loss in a single crystal is the observable in CATANA and it corresponds to the kinetic energy of the proton.

Protons pass through various materials before entering CATANA crystals and lose their energy. Therefore, the observable energy of the proton is lower than its initial energy. This effect is discussed in Sec. 5.3.

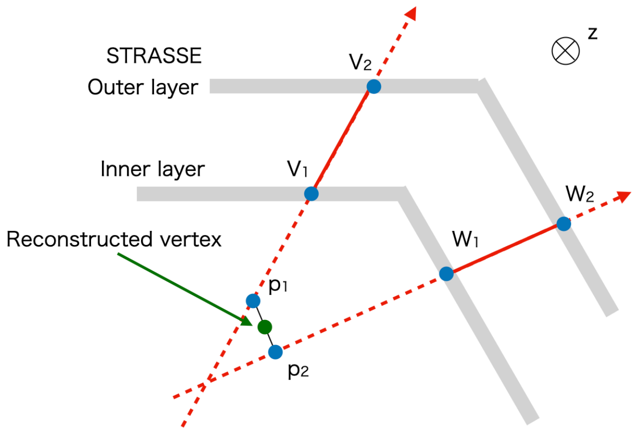

Figure 5.3: Schematic of vertex reconstruction. The direction of the beam is perpendicular to the paper.

Vertex reconstruction

When two tracks are detected by STRASSE, the position of the vertex can be reconstructed. The information about the vertex is utilized in the vertex selection (described in Sec. 5.2) and the energy loss correction (described in Sec. 5.3).

The schematic of vertex reconstruction is shown in Fig. 5.3. The passing points of two protons in each layer are defined as V_1, V_2, W_1, W_2. p_1 and p_2 are the points on the $\overrightarrow{V_1V_2}$ and $\overrightarrow{W_1W_2}$ respectively. The coordinates of p_1 and p_2 are calculated to minimize the distance between p_1 and p_2. The reconstructed vertex is given by the middle point of p_1 and p_2.

Figure 5.4 shows the distribution of the distance between the true vertex and the reconstructed vertex. 68.3% (1σ) of the reconstructed vertices are within 0.83 mm.

5.2 Selection Criteria

Various criteria are applied to select two recoil protons. The details of each selection cuts are described below.

Edge cut

There exsits the events that the one of the recoil proton pass through the support frame of the STRASSE. It is difficult to estimate the energy loss of the recoil proton in such an event, and hence these events are removed. Five longitudinal strips at both ends and ten transeverse strips at the beam direction end is ignored in each STRASSE wafer (Fig. 5.5).

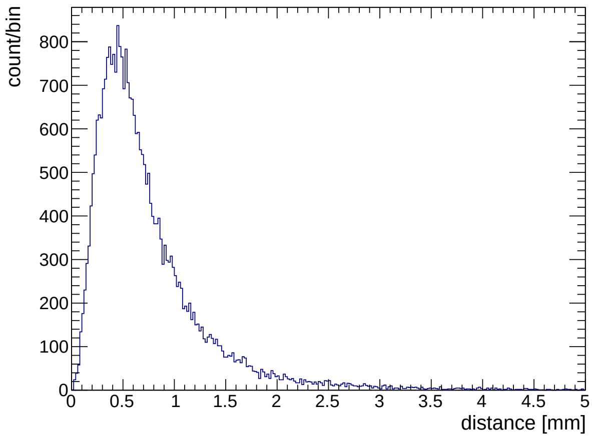

Figure 5.4: Simulated distance between true vertex and reconstructed vertex. True $E_{\mathrm{x}} = 30\,\mathrm{MeV}$.

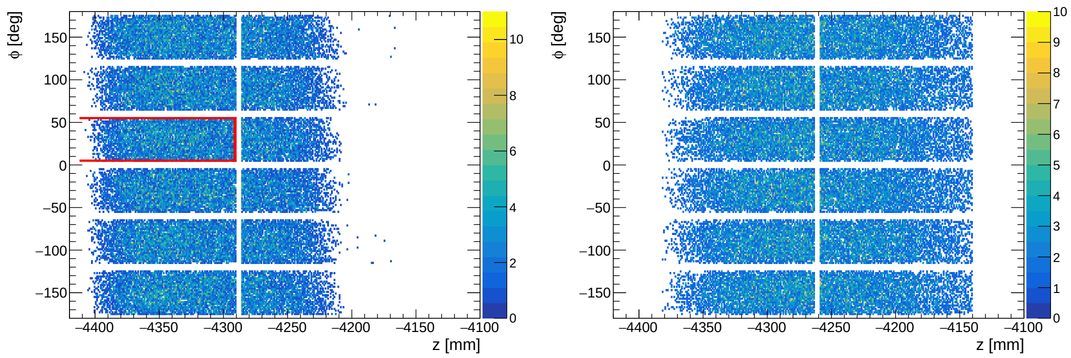

(a) Inner layer

(b) Outer layer

Figure 5.5: Simulated passing point of the recoil protons on the STRASSE (a) inner and (b) outer layers. The red area indicates one of the cut region.

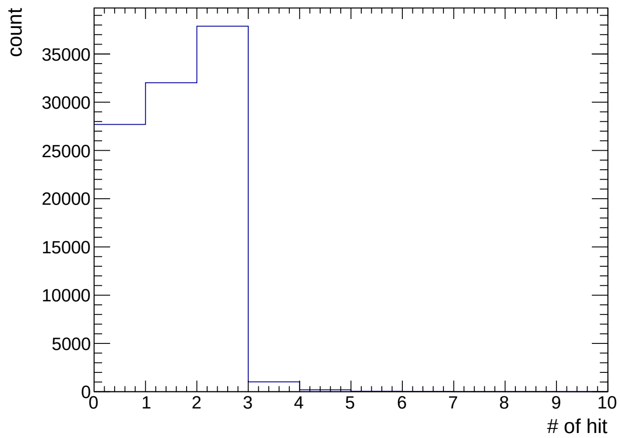

Figure 5.6: Simulated number of the tracks detected by STRASSE. $E_{x,\mathrm{true}} = 30\,\mathrm{MeV}$.

Track selection

When the inner layer and the outer layer with the same azimuthal angle coverage in STRASSE detect charged particles, their signals are considered due to a single track. Figure 5.6 shows the number of the tracks detected by STRASSE. Events with two reconstructed tracks are selected.

Vertex selection

Figure 5.7 shows the distribution of the reconstructed vertex. 98% of the reconstructed vertices are inside the target. There are two main reasons that some of the reconstructed vertices are outside the target. First, the reconstructed vertex lies just outside the target due to proton straggling. Second, the reconstructed vertex lies on the outer layer. This mis-reconstruction happens when two particles pass though the same inner layer but only one particle pass through the outer layer. In order to reject these events, events with the reconstructed vertex within the target are selected.

Angular selection

At the center-of-mass frame, the two recoil protons are emitted back to back. In the lab frame, two protons are boosted in the beam direction and have a back-to-back correlation in the azimuthal direction. Therefore, events with two proton azimuthal angle $\phi = 180° \pm 36°$ in CATANA are selected (Fig. 5.8).

Energy selection

Figure 5.9 shows the simulation energy desctibution detected by CATANA. The low energy region is due to gamma-ray contribution, which is mainly produced by the secondary reactions. In order to reject gamma-rays, events where both energies exceed 10 MeV are selected.

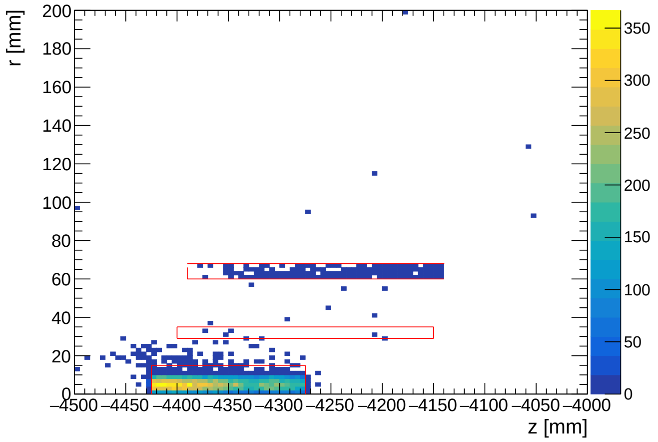

Figure 5.7: Simulated positions of the reconstructed vertex by STRASSE. The red boxes represent the outer layer, the inner layer and the target from the top. $E_{x,\mathrm{true}} = 30\,\mathrm{MeV}$.

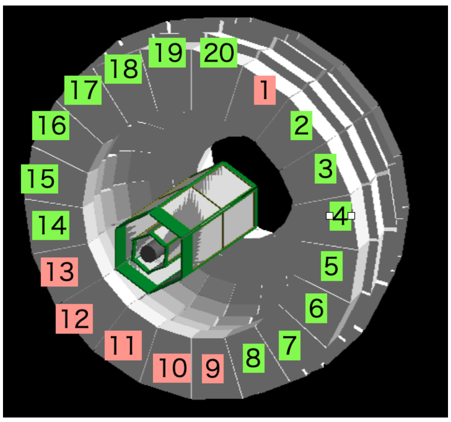

Figure 5.8: Illustration of event selection with CATANA. When there is a hit on crystal 1, the event with a hit on either crystal 9 to 13 is selected.

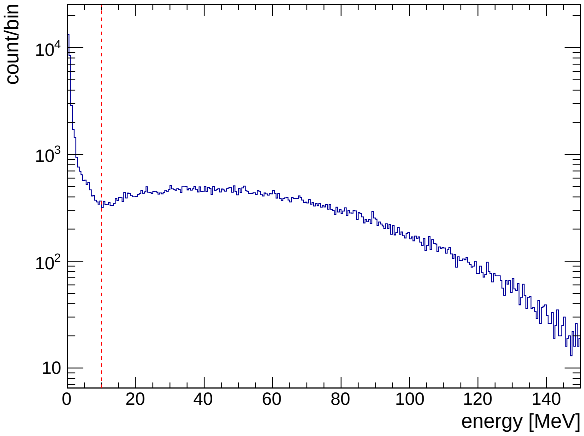

Figure 5.9: Simulated energy distribution detected by CATANA. The vertical dashed line indicates the energy threshold. $E_{x,\mathrm{true}} = 30\,\mathrm{MeV}$.

Table 5.1: Simulated efficiency of the $^{16}\mathrm{O}(p,2p)^{15}\mathrm{N}$ selection for all $^{16}\mathrm{O}(p,2p)^{15}\mathrm{N}$ events within the target at given excitation energies.

Selection	Efficiency [%]		
	$E_\mathrm{x} = 10\,\mathrm{MeV}$	30 MeV	50 MeV
Edge cut & Track selection	33.7	28.6	19.5
Vertex selection	33.1	27.9	18.9
Angular selection	17.1	14.1	9.6
Energy selection	15.8	12.7	8.5
Matching of STRASSE and CATANA	9.5	7.7	5.2

Matching of STRASSE and CATANA

Tracks reconstructed by STRASSE and energies detected by CATANA are matched. The track reconstructed by STRASSE is extrapolated and if the track hits the CATANA crystal which has hit, it is assumed that these signals are produced by the same proton. The momentum direction of the proton is acquired by STASSE and the kinetic energy of it is acquired by CATANA. Consequently, the four momentum of the recoil proton is reconstructed. Events with two matched tracks are selected.

Table 5.1 shows the efficiency of the $^{16}\mathrm{O}(p,2p)^{15}\mathrm{N}$ selection for all $^{16}\mathrm{O}(p,2p)^{15}\mathrm{N}$ events within the target at given excitation energies. The polar angle of the recoil proton descreases as the excitation energy increases. As the excitation energy increases, the number of recoil protons with a smaller polar angle increases. Since STRASSE and CATANA cover $20^\circ \lesssim \theta \lesssim 60^\circ$, the efficiency descreases for the higher excitation energy.

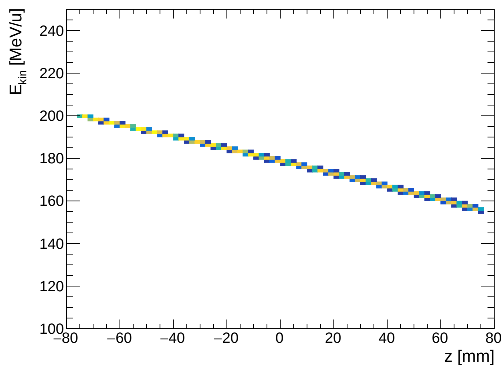

Figure 5.10: Correlations between the z-position of the vertex and the kinetic energy of the beam. $z = -75$ and $z = +75$ are the upstream and downstream ends of the target.

5.3 Energy Loss Correction of Oxygen Beam

Oxygen beam loses its kinetic energy as it pass through the LH_2 target and then the kinetic energy just before the reaction is lower than its incident energy, 200 MeV/u. This energy loss was estimated by shooting 200 MeV/u oxygen beam into the LH_2 target in the simulation. The kinetic energy of the oxygen beam just before the reaction is shown in Fig. 5.10. Its energy loss is about 0.3 MeV/u per 1 mm.

The kinetic energy of the oxygen beam just before the reaction E_{kin} is estimated from the z-cordinate of the reconstructed vertex z as follows:

$$E_{\mathrm{kin}}\,[\mathrm{MeV/u}] = 200 - 0.3 \times (z - z_{\mathrm{upstream}})\,[\mathrm{mm}] \tag{5.1}$$

where z_{upstream} is the z-cordinate of the upstream ends of the target.

5.4 Energy Loss Correction of Recoil Protons

The recoil protons lose energy before entering the CATANA crystals. Energy loss of recoil protons is corrected by utilizing the path length estimated from the reconstructed vertex position.

5.4.1 Estimation of Path Length

Recoil protons pass through various materials before being detected by CATANA as shown in Fig. 5.11. The materials and typical path lengths are listed in Table 5.2. The path length of recoil protons is estimated from the reconstructed vertex position.

LH_2 target

Recoil protons pass through the target diagonally, and their typical path length are around 20 mm. The path length in the target is estimated from the vertex and

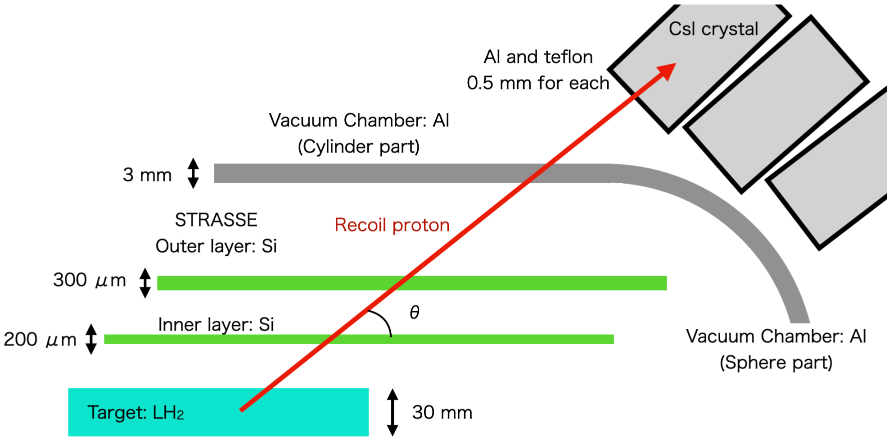

Figure 5.11: Illustration of the energy loss of the recoil protons.

Table 5.2: The materials through which recoil protons pass. Stopping powers are calculated by [29].

Material	Path length [mm]	Density [g/cm^2]	Stopping power at 100 MeV [MeV cm^2/g]
LH_2 target	10 - 30	0.0729	15.30
Si layer	0.5 - 1.0	2.33	5.838
Al vacuum chamber	3	2.70	5.678
Al housing of CsI crystals	0.5	2.70	
Teflon reflector of CsI crystals	0.5	2.2	6.077

the momentum direction reconstructed by STRASSE.

Si **layer**

Since recoil protons pass through the layer diagonally, the incident angle to the layers is considered. The path length in the Si layers is $500/\sin\theta\,\mu\text{m}$, where θ is the elevation angle of the track detected by STRASSE.

Al **vacuum chamber**

If the recoil proton is estimated to pass through the cylinder part of the chamber, its incident angle is considered. If the recoil proton is estimated to pass through the sphere part, it is assumed that path length is 3 mm.

Al **housing and teflon reflector of** CsI **crystals**

It is assumed that protons pass perpendicularly through the housing and reflector, with a path length of 0.5 mm for each.

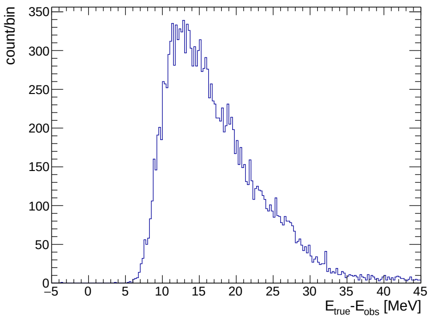

(a) Before correction

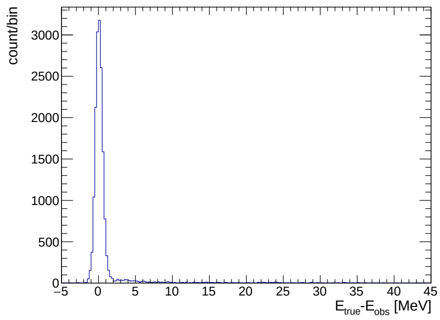

(b) After correction

Figure 5.12: Difference between initial kinetic energy (true information) and observable kinetic energy of recoil proton.

5.4.2 Energy Loss Correction of Recoil Protons

From the path length Δx and the kinetic energy after passing the material E_{after}, the kinetic energy before passing the material E_{before} is estimated as:

$$E_{\text{before}} = E_{\text{after}} + \frac{dE}{dx}(E_{\text{after}}) \times \Delta x, \tag{5.2}$$

where dE/dx is the stopping power calculated by the PSTAR program [29] based on the Bethe-Bloch formula. The initial kinetic energy is reconstructed by repeating this process for the matirials on the path, from the one closest to the CATANA crystal and then towards the target.

Figure 5.12a shows the difference between truth initial kinetic energy and observable energy by CATANA. The observable energies are around 10 MeV lower than their initial kinetic energies due to the energy loss. By applying the energy loss correction described above, the initial kinetic energy of the proton is estimated. Figure 5.12b shows the difference between initial kinetic energy and reconstructed kinetic energy. Most of the protons are well corrected: energy difference is within 2 MeV. However, there are still 8.5% of protons whose energy loss is more than 2 MeV larger than the estimation. The causes of this are discussed in Sec. 5.6.2.

5.5 Excitation Energy Reconstruction

The excitation energy of ^{15}N is reconstructed by the missimg mass method. It is calculated using the following formula (same as Eq. (3.1)):

$$E_{\text{x}} = \sqrt{(E_{\text{beam}} + E_{\text{tgt}} - E_1 - E_2)^2 - (\vec{P}_{\text{beam}} - \vec{P}_1 - \vec{P}_2)^2} - M_{\text{frag}} \tag{5.3}$$

where E_{beam}, E_{tgt}, E_1, E_2 are the energy of the oxygen beam, target proton and two recoil protons, respectively. $\vec{P}_{\text{beam}}$, $\vec{P}_1$, $\vec{P}_2$ are the momentum of the oxygen beam and two recoil protons, respectively. The momentum direction of the oxygen beam ($\vec{P}_{\text{beam}}$) is assumed to be parallel with the z-axis. The energy of the oxygen beam

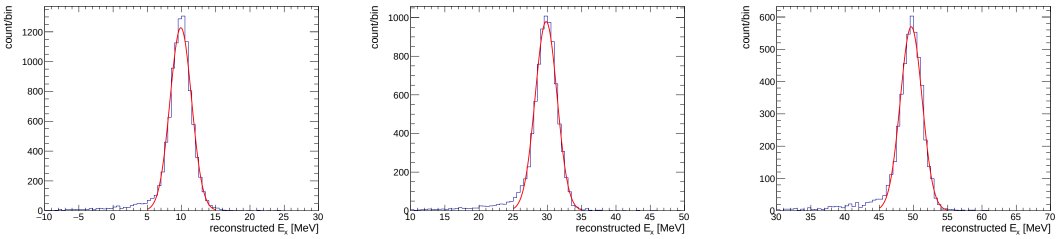

(a) True $E_{\mathrm{x}} = 10\,\mathrm{MeV}$ (b) True $E_{\mathrm{x}} = 30\,\mathrm{MeV}$ (c) True $E_{\mathrm{x}} = 50\,\mathrm{MeV}$

Figure 5.13: Distribution of reconstructed excitation energy. The red line represents the fitting result with a Gaussian.

Table 5.3: The result of the excitation energy reconstruction. The range of the Gaussian fitting is $[E_{x,\mathrm{true}} - 5,\ E_{x,\mathrm{true}} + 5]$. The ratio of the tail components is defined as the percentage of the events below $E_{x,\mathrm{true}} - 5$ to the total reconstructed events.

	Gaussian fitting		Tail conponents
True E_{x} [MeV]	Mean [MeV]	σ [MeV]	Ratio [%]
10	9.9	1.6	5.5
30	29.8	1.6	6.6
50	49.6	1.6	7.2

(E_{beam}) is estimated from the reconstructed vertex. The momentum directions of recoil protons ($\vec{P}_1/|\vec{P}_1|$, $\vec{P}_2/|\vec{P}_2|$) are measured by STRASSE. The kinetic energies of two recoil protons (E_1, E_2) are measured by CATANA and the effects of their energy losses are considered.

The distribution of the reconstructed excitation energy is shown in Fig. 5.13. The result of a Gaussian fitting is shown in Table 5.3. The sigmas of the Gaussian are 1.6 MeV for all three excitation energy. The main factor contributing the excitation energy resolution is discussed in Sec. 5.6.1. There are tail conponents in the lower region and then the means of the Gaussian are shifted to lower. The causes of this are discussed in Sec. 5.6.2.

5.6 Discussion

5.6.1 Main Factor Determining the Resolution

We found that the excitation energy resolution is mainly determined by the angular resolution of STRASSE by the following studies. In order to evaluate the contribution to the excitation energy resolution, one of the observables is replaced by the true value and the excitation energy is recalculated. Figure 5.14b shows the distribution of reconstructed excitation energy when the true momentum directions of the recoil protons are used in the calculation. The observable momentum direction is used in the vertex reconstruction and energy loss correction. The stan-

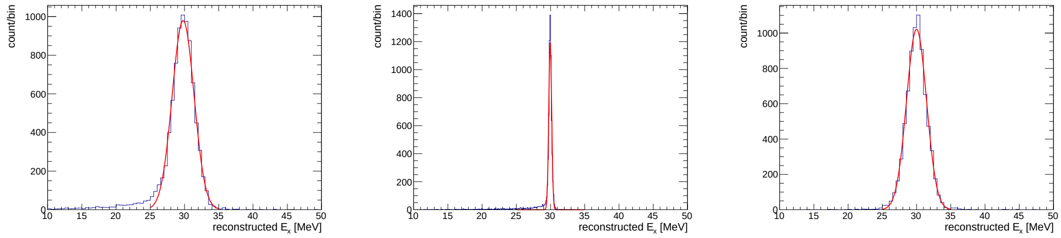

(a) Nominal (b) Momentum direction (c) Kinetic energy

Figure 5.14: Distribution of reconstructed excitation energy. The red line represents the fitting result with a Gaussian. (a) is obtained by the nominal reconstruction method (same as Fig. 5.13b). (b) is obtained by replacing the observable momentum directions to the initial momentum directions. (c) is obtained by replacing the observable kinetic energies to the initial kinetic energies.

Table 5.4: The angular resolution of recoil protons with kinetic energy of 125 MeV emitted at 45° passing by a system including an LH_2 target and a silicon tracker in vaccum. The value is taken from [26].

Factor		σ_θ [mrad]
LH_2 target	Radious of 15.5 mm	3.0
Si inner layer	Thickness of 200 µm	3.3
Si inner layer	Pitch size of 200 µm	1.0
Total		4.9

dard deviation of the Gaussian is 0.2 MeV. Figure 5.14c shows the distribution of reconstructed excitation energy when the true kinetic energies of the recoil protons are used in the calculation. The standard deviation of the Gaussian is 1.5 MeV. Therefore, it can be concluded that the angular resolution of STRASSE determines the resolution of the excitation energy.

The angular resolution of STRASSE is studied by [26]. Table 5.4 shows the angular resolution of recoil protons calculated by [26]. The straggling in the LH_2 target and the inner layer mainly contributes to the angular resolution of STRASSE and both contributions are almost the same. Although the finite pitch size of the strip can worsen the angular resolution, this contribution is small compared to the other two factors.

Figure 5.15a shows the distribution of the angle between the initial momentum direction and the observable momentum direction of recoil protons. The region below 11.1 mrad contains 68.3% (1σ) of the entries. This value is higher than that of Table 5.4. This is because the kinetic energy of the proton is lower than that of Table 5.4. Figures 5.15b and 5.15c show the angle between the initial momentum direction and the observable momentum direction for the proton whose kinetic energy is below and above 70 MeV. The straggling becomes larger as the kinetic energy of the proton is lower. The region below 8.5 mrad (13.5 mrad) for protons with kinetic energies above (below) 70 MeV contains 68.3% (1σ) of the entries.

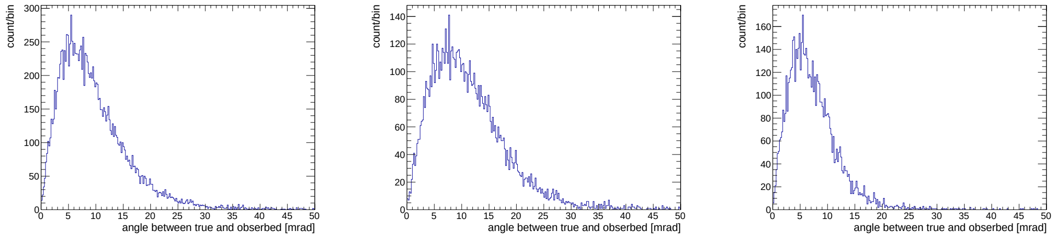

(a) All (b) $E_{\text{kin}} < 70\,\text{MeV}$ (c) $E_{\text{kin}} > 70\,\text{MeV}$

Figure 5.15: Angle between the initial momentum direction and the observable momentum direction. The true excitation energy is 30 MeV.

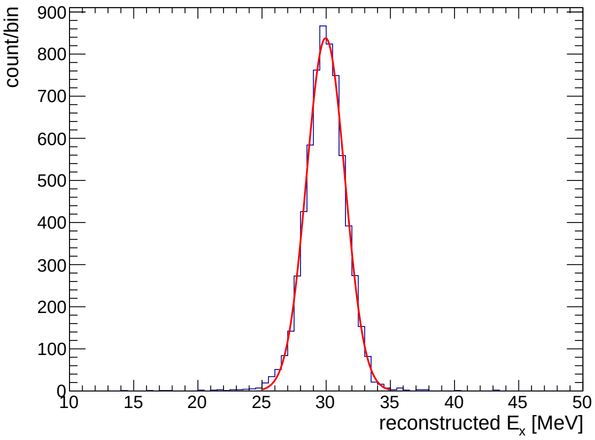

Figure 5.16: Distribution of reconstructed excitation energy. The events that one of the observable energy of the recoil proton is 2 MeV lower than its initial energy are removed.

5.6.2 Cause of the Tail Components

There are tail components at the distributions of reconstructed excitation energy (Fig. 5.13). This is because of the underestimation of the kinetic energy of recoil protons. Although the energy loss of recoil protons is estimated and corrected, protons with energies differing by more than 2 MeV accounted for 8.5% of the total protons at true $E_{\text{x}} = 30\,\text{MeV}$(Fig. 5.12b). When the events that one of the observable energy of the recoil proton is 2 MeV lower than its true energy are removed, the tail components are disappeared (Fig. 5.16).

The causes of the underestimation can be categorized as follows:

1. Proton escaped from a single CATANA crystal and did not deposit all energy.

   Since the range of 100 MeV proton is about 30 mm and CATANA crystal is about 100 mm length, most of the proton stops in a single crystal. However, some protons escape a crystal when they enter near the edge of the crystal. This makes the observable energy lower than its true energy.

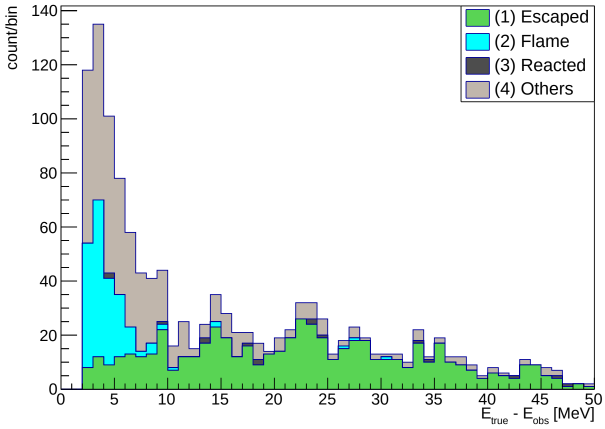

Figure 5.17: Difference between the initial kinetic energy and the observable kinetic energy of recoil protons.

2. Proton passed through the frame of STRASSE.
   The energy loss of the STRASSE frame is not considered in this study. If the proton pass through the STRASSE frame, the observable energy is lower than its true energy.

3. Proton reacted with a material and its products entered into a CATANA crystal.
   Some protons react with a material and produce secondary particles. They enter into a CATANA crystal and are misunderstood as protons.

4. Others.
   There are Al housings and teflon reflectors in the gaps between the CATANA crystals. One possible scenario is that protons may pass through these spaces, lose extra energy, and then enter the crystal.

Figure 5.17 shows the difference between the initial kinetic energy and the observable kinetic energy of recoil protons colored according the factors. The largest contribution comes from the case where the protons escaped from CATANA.

5.7 Excitation Energy Reconstruction for Continuous Input Distribution

In the previous sections, the excitation energy of ^{15}N is fixed. In this section, the excitation energy reconstruction with the continuous excitation energy distribution is discussed. We plan to measure the excitation energy for 5 MeV bin in the SAMURAI-79 experiment. The contamination from adjacent bins is evaluated with the event generated based on the Benhar's spectral function (described in Sec. 4.2).

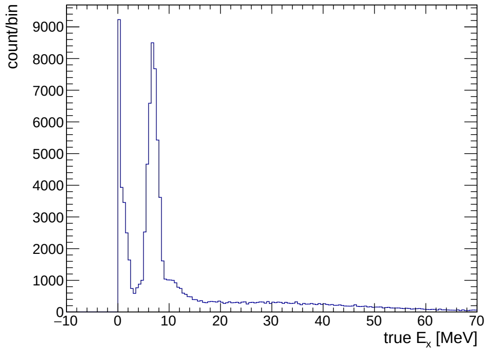

(a) True.

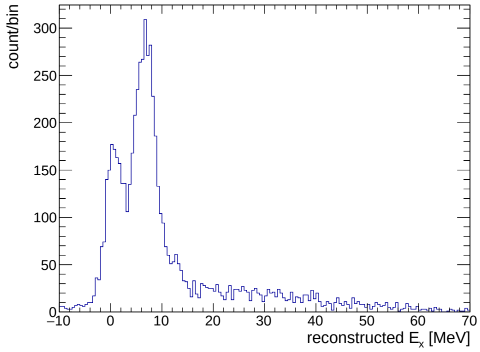

(b) Reconstructed.

Figure 5.18: Simulated distribution of true and reconstructed excitation energy.

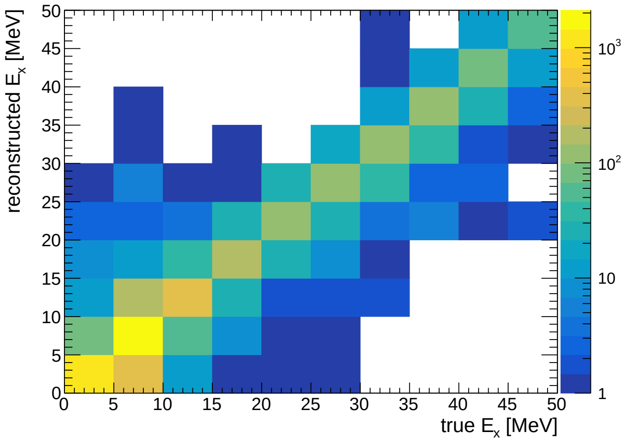

Figure 5.19: Simulated two dimensional distribution of true and reconstructed excitation energy.

The simulation and reconstruction methods are the same as those used for the fixed excitation energy. Two recoil protons are shot in the simulation and the detector response is simulated. Figure 5.18a and Fig. 5.18b show the true and reconstructed excitation energy distribution, respectively. The two dimensional distribution of true and reconstructed excitation energy for a 5 MeV bin is shown in Fig. 5.19.

The purity for each excitation energy bin is defined as:

$$(\text{Purity}) = \frac{(\#\text{ of events where both the true and reconstructed excitation energies are within the bin})}{(\#\text{ of events for which the reconstructed excitation energy is within the bin})}. \tag{5.4}$$

The purity for each bin is listed in Table 5.5. In the region of interest to us, $10 < E_\mathrm{x} < 50\,\mathrm{MeV}$, the purity is approximately 60-70%. The purity of the $5-10\,\mathrm{MeV}$

Table 5.5: Simulated purity for each excitation energy bin.

Reconstructed Ex bin	Purity (%)
0 - 5	71
5 - 10	93
10 - 15	60
15 - 20	65
20 - 25	63
25 - 30	62
30 - 35	69
35 - 40	74
40 - 45	72
45 - 50	72

bin is high because there is a peak of $p_{3/2}$ shell level. On the other hand, the purity of the $10-15$ MeV bin is low because of the contamination from the peak of $p_{3/2}$ shell level. The tail component discussed in Sec. 5.6.2 is contaminated from the upper bin. Since the number of events decreases at higher excitation energy, the purity is higher in the high excitation energy bin. It is important to precisely estimate these contamination and correct them.

Chapter 6

Measurement of De-excitation Process

In this chapter, a study for the measurement of the de-excitation products from ^{15}N is described.

We aim to measure the branching ratios of the major channels from the de-excitation of ^{15}N. The branching ratio predicted by various models are compared in Sec. 6.1. The branching ratio is measured by detecting residual nuclei and evaporated neutrons. The optimization of the magnetic field for measuring residual nuclei is described in Sec. 6.2. The detection efficiency of evaporated neutrons is described in Sec. 6.3.

6.1 Branching Ratio Predictions

6.1.1 Branching Ratio predictions

Three de-excitation simulation programs, G4PreCompound in Geant4 [23], ABLA [37] and YAHFC [47] are compared in this thesis. They refer to different models and describe the de-excitation of an excited nucleus through the emission of gamma-rays, neutrons, and light charged particles. G4PreCompound and ABLA are the de-excitation codes provided by Geant4. G4PreCompound simulates the de-excitation of light nuclei ($Z \leq 9$ and $A \leq 17$) based on Fermi breakup model[48]. ABLA is based on Weisskopf's formalism[49]. YAHFC (Yet Another hauser Feshbach Code) is a computer program framework to model low-energy nuclear reactions based on the compound-nucleus hypothesis and the statistical decay of Hauser-Feshbach model.

6.1.2 Comparison of branching ratios for various models

The branching ratios of the major channels from the de-excitation of ^{15}N for the various predictions are shown in Table 6.1. The excitation energy distribution is based on the Benhar's spectral function (Sec. 4.2). The excitation energy range is set to $10.83 < E_{\mathrm{x}} < 50\,\mathrm{MeV}$. The lower bound of 10.83 MeV is determined based

Table 6.1: The branching ratio of the de-excitation of ^{15}N for the various prediction. The excitation energy of ^{15}N is distributed based on the spectral function and its range is $10.83 < E_{\mathrm{x}} < 50$ MeV. The blank row channels in YAHFC are included in Others.

	Branching ratio [%]		
Channel	G4PreCompound	ABLA	YAHFC[1]
$^{14}\mathrm{N} + n$	38.1	30.3	26.5
$^{13}\mathrm{C} + p + n$	11.2	9.8	13.6
$^{11}\mathrm{B} + \alpha$	6.7	6.4	8.8
$^{6}\mathrm{Li} + 2\alpha + n$	6.4	8.6	
$^{12}\mathrm{C} + p + 2n$	6.2	5.2	8.7
$^{12}\mathrm{C} + d + n$	5.6	3.8	6.1
$^{7}\mathrm{Li} + 2\alpha$	5.5	3.0	
$^{14}\mathrm{C} + p$	3.9	6.7	12.1
$^{13}\mathrm{N} + 2n$	3.8	1.2	5.0
Others	12.6	26.0	19.2

Table 6.2: The major charged particles produced by the de-excitation of ^{15}N.

Particles	A/Z
p	1
^{13}C	13/7
^{14}N, ^{12}C, ^{6}Li, α, d	2
^{13}C	13/6
^{11}B	2.2
^{14}C, ^{7}Li	7/3

on the separation energy of neutron, $S_n = 10.83$ MeV since we are interested in the de-excitation with a particle emission. The upper bound of 50 MeV is set since the number of events is limited. The gamma-rays are omitted in this table.

G4PreCompound and ABLA stop the calculation when the nuclei transition to their ground states. ^{8}Be is unstable nuclei and decays to 2α in a lifetime of 0.08 ps[50], which happens before it leaves the target. When ^{8}Be is produced by G4PreCompound and ABLA, it is assumed that ^{8}Be immediately decays into 2α.

The branching ratio is largely different depending on the prediction. The mean neutron multiplicity is 0.892, 0.800 and 0.865 for G4PreCompound, ABLA, and YAHFC, respectively.

6.2 Measurement of Residual Nuclei

Table 6.2 shows the major charged particles produced by the de-excitation of ^{15}N. We plan to detect the residual nuclei ranging from $A/Z = 13/7$ (^{13}C) to 7/3 (^{14}C).

[1] The simulation of YAHFC was performed by R. Akutsu.

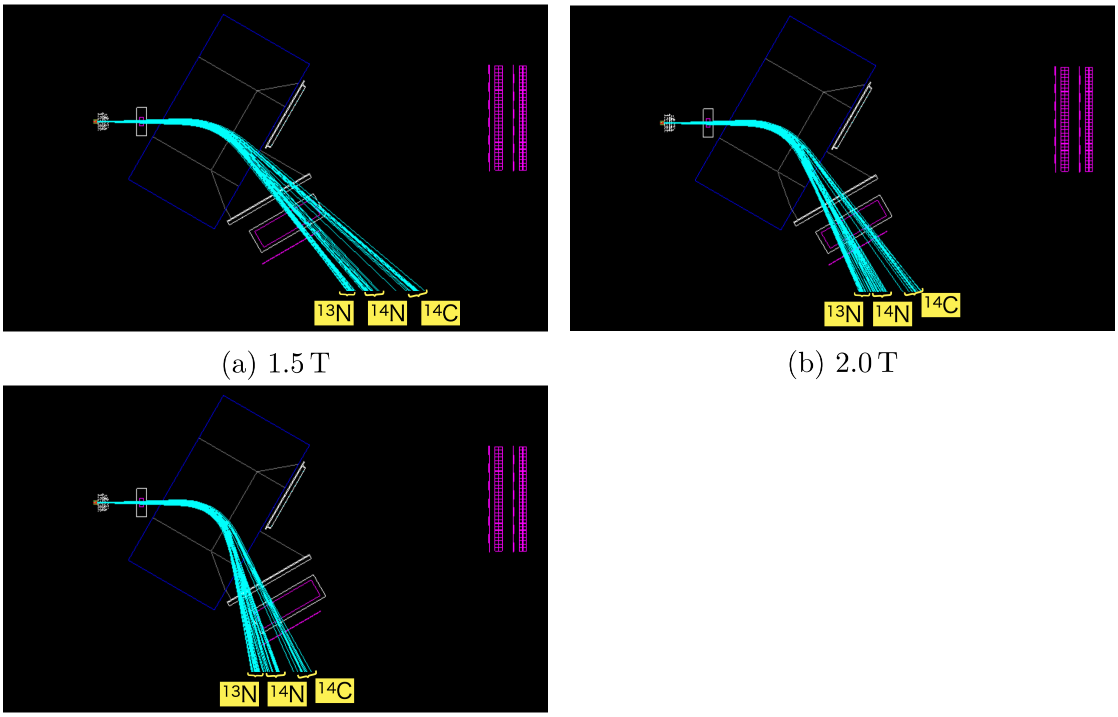

(a) 1.5 T

(b) 2.0 T

(c) 2.5 T

Figure 6.1: Simulated tragectories of ^{13}N, ^{14}N and ^{14}C in a different magnet field. These nucleus are produced by the de-excitation of ^{15}N from the ^{16}O$(p, 2p)^{15}$N reaction at 200 MeV/u.

These nuclei are detected by the charged particle detectors: FDC1, FDC2, and HODF24 (Sec. 3.2) and identified based on the curvature of their trajectories in the magnetic field. Figure 6.1 shows the simulated tragectories of ^{13}N (smallest A/Z), ^{14}N, and ^{14}C (largest A/Z). The magnetic fields of 1.5 T, 2.0 T and 2.5 T are tested. All the trajectories of the residual nucleus lie within the detector acceptance when the magnetic field of 2.0 T. Therefore the magnetic field of 2.0 T is selected.

6.3 Measurement of Evaporated Neutrons

Evaporated neutrons are detected by NEBULA, plastic scintillator array located downstream of the magnet (Sec. 3.2). Information of neutrons can be used to determine the de-excitation channel which cannot be distinguished from information of the residual nuclei only. For example, when ^{12}C is detected by the charged particle detectors, there are three possible channels, $^{12}\mathrm{C} + t$, $^{12}\mathrm{C} + d + n$, and $^{12}\mathrm{C} + p + 2n$. These channels are distinguished by counting the number of neutrons by NEBULA.

The neutron detection efficiency is evaluated with a channel that has the largest branching ratio, $^{14}\mathrm{N} + n$. The ^{16}O$(p, 2p)^{15}$N reactions at 200 MeV/u are generated based on the spectral function. The ^{14}N, the neutron and the gamma-rays from the

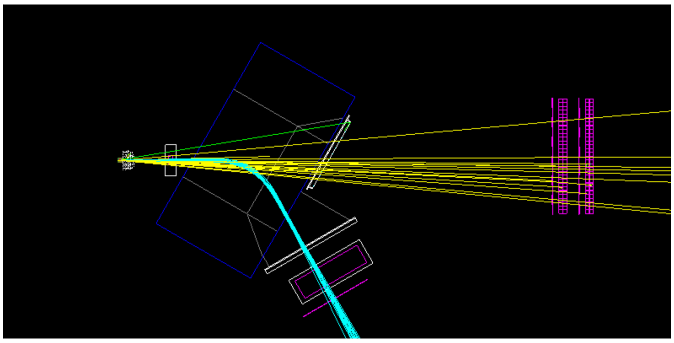

Figure 6.2: Simulated trajectories of the ^{14}N (blue lines) and the neutrons (yellow lines).

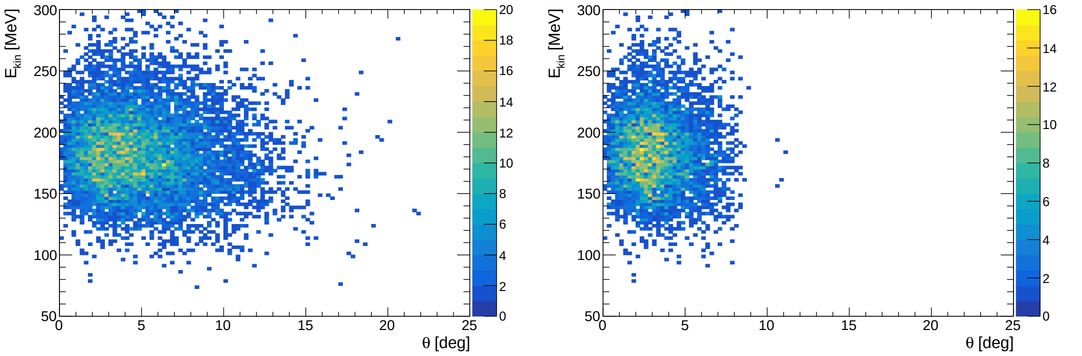

(a) All neutrons. (b) Neutrons which hit NEBULA.

Figure 6.3: Simulated distributions of the initial kinetic energy and the polar angle of the neutron in the lab frame.

$^{14}\mathrm{N} + n$ event are emitted in the simulation, and the response of NEBULA is simulated (Fig. 6.2). The energy threshold is set to be 6 MeVee (electron equivalent) to remove the gamma-rays.

Figures 6.3 and 6.4 show the initial kinetic energy and the polar angle of the neutron in the ^{15}N rest frame and the lab frame, respectively. The most kinetic energy of the neutron is below 10 MeV in the rest frame. The neutrons are emitted isotropically in the rest frame. The neutrons which have large polar angle above $\theta = 8°$ (for $\phi = 0°, 180°$) and $\theta = 4°$ (for $\phi = \pm 90°$) in the lab frame cannot hit NEBULA, where ϕ is the azimuthal angle and $\phi = 0°$ corresponds to the upward direction in Fig. 6.2. These neutrons account for about 40% of all neutrons. Some neutrons are detected by NEBULA even though geometrically they don't hit NEBULA. These neutrons undergo elastic scattering within the target or other materials in the simulation, and reach NEBULA.

Figure 6.5 shows the distribution of multiplicity, defined as the number of hit detectors with a light output lager than 6 MeVee. The result is summarized in Table 6.3. 22% of the events have more than one hit detectors. The neutron detection efficiency is defined as the ratio of events with one hit. An efficiency of

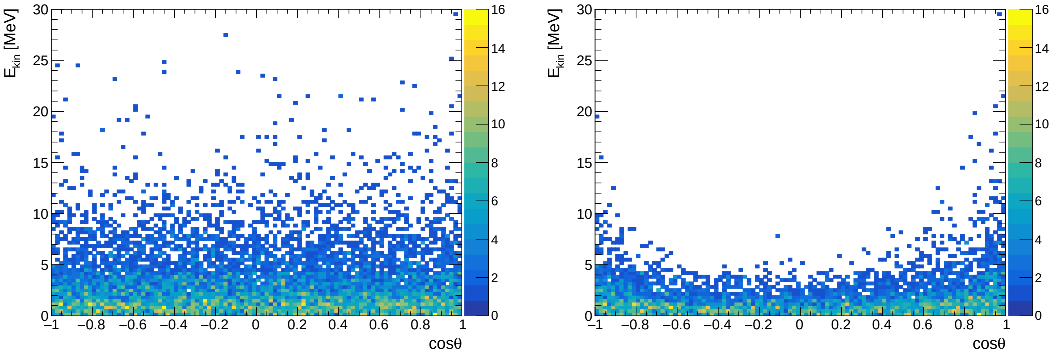

(a) All neutrons. (b) Neutrons which hit NEBULA.

Figure 6.4: Simulated distributions of the initial kinetic energy and the polar angle of the neutron in the rest frame of ^{15}N.

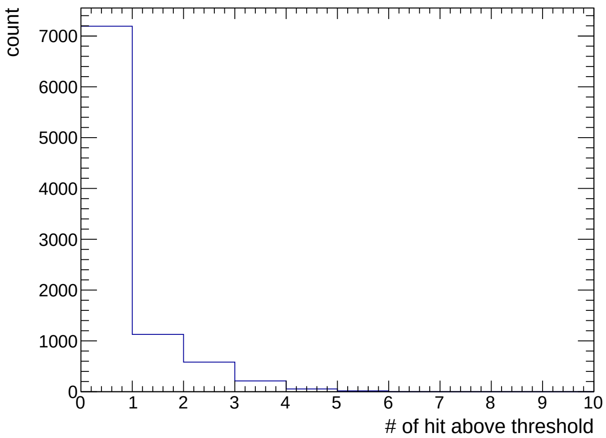

Figure 6.5: Simulated multiplicity distribution.

12% is obtained in this simulation. This value is lower than that of the previous measurement, 32.5%[42]. There are two reasons. Fisrt, the previous result is obtained by $^{7}\mathrm{Li}(p,n)^{7}\mathrm{Be}$ reaction with a 200 MeV proton beam. This reaction produces neutron with large zero-degree cross section and most neutron can reach NEBULA. On the other hand, the evaporated neutrons simulated in this study have relatively large polar angles and about 40% of neutrons geometrically cannot reach NEBULA. Second, there are events where a single neutron produces more than one signal that mimic multi-neutron events. This event is called cross-talk event. By correctly distinguishing between the cross-talk events and multi-neutron event, the efficiency can be increased by up to 22%. This process is called cross-talk rejection[41] and applied to the previous measurement.

Table 6.3: Simulated ratio for all event.

Conditions	Ratio [%]
Neutrons geometrically able to reach NEBULA	60
More than one hit detectors	22
One hit detector	12

Chapter 7

Expected Impact and Future Prospects

7.1 Estimation of the Statistical Performance of the Measurement of Branching Ratio

The expected statistical performance of the branching ratio measurement is estimated for the major de-excitation channels.

We plan to run with a beam intensity of 1×10^5 pps over 4 hour beam time. The efficiency of the $^{16}\mathrm{O}(p, 2p)^{15}\mathrm{N}$ selection for all $^{16}\mathrm{O}(p, 2p)^{15}\mathrm{N}$ events at $E_\mathrm{x} = 30\,\mathrm{MeV}$ is estimated to be 7.7% in this study (obtained from Sec. 5.2). The density of the $\mathrm{LH_2}$ target is $0.073\,\mathrm{g/cm^3}$ and the length is 150 mm, corresponding to 6.6×10^{23} atoms per cm^2. Assmuing that the DAQ live time fraction (LT) is 80% and the cross section for producing an excited states of $^{15}\mathrm{N}$ by a $^{16}\mathrm{O}(p, 2p)$ reaction is 6 mb[1], the number of $^{16}\mathrm{O}(p, 2p)^{15}\mathrm{N}$ events obtained by this experiment is

$$4\,\mathrm{h} \times 0.8\,(LT) \times 7.7\% \times 6\,\mathrm{mb} \times (6.6 \times 10^{23}\mathrm{cm}^{-2}) \times (1 \times 10^5\,\mathrm{pps}) = 3.5 \times 10^5\,\mathrm{events}. \tag{7.1}$$

The detection efficiency of residual nuclei is empirically 95%. The branching ratio of $^{14}\mathrm{N} + n$ for $10.83 < E_\mathrm{x} < 50\,\mathrm{MeV}$ is 38.1% in G4PreCompound (obtained from Sec. 6.1). Therefore, the number of $^{14}\mathrm{N}+n$ events detected by this experiment is estimated to be

$$(3.5 \times 10^5\,\mathrm{events}) \times 38.1\% \times 95\% = 1.3 \times 10^5\,\mathrm{events}, \tag{7.2}$$

corresponding to a statistical uncertainty of 0.3%.

Three channel, $^{12}\mathrm{C}+t$, $^{12}\mathrm{C}+d+n$, and $^{12}\mathrm{C}+p+2n$ are distinguished by counting the number of neutrons. The branching ratio of $^{12}\mathrm{C}+d+n$ for $10.83 < E_\mathrm{x} < 50\,\mathrm{MeV}$ is 5.6% in G4PreCompound (obtained from Sec. 6.1). Assmuing that the detection efficiency of neutrons from $^{12}\mathrm{C}+d+n$ is the same as that of $^{14}\mathrm{N}+n$, 12% (obtained from Sec. 6.3), the number of neutron from $^{12}\mathrm{C}+d+n$ detected by this experiment is estimated to be

$$(3.5 \times 10^5\,\mathrm{events}) \times 5.6\% \times 95\% \times 12\% = 2.2 \times 10^3\,\mathrm{neutrons}, \tag{7.3}$$

[1] The cross section is calculated by K. Ogata

corresponding to a statistical uncertainty of 2.1%.

7.2 Impact on DSNB Search

We aim to reduce the systematic uncertainties in the atmospheric neutrinos background in the DSNB seach at SK. The effect of these uncertainties on the DSNB sensitivity is evaluated.

In the systematic uncertainties on the NCQE events listed in Table 2.2, this experiment contributes to reduce the systematic uncertainties of NCQE cross section, neutron multiplicity, and spectral shape. In the systematic uncertainties on the non-NCQE events listed in Table 2.3, this experiment contributes to reduce the systematic uncertainty of neutron multiplicity. In Sec. 7.1, the statistical uncertainty below 10% is obtained. Therefore, although the DSNB analysis is complicated and difficult to estimate the effect on uncertainties, we assume that we can reduce the systematic uncertainty of both NCQE and non-NCQE events to 20%. The expected sensitivity of DSNB is calculated if both the systematic uncertainties for NCQE and non-NCQE is 20%. In addition, other works to reduce the other uncertainties such as atmospheric neutrino flux in NCQE are on going. The uncertainty of the scaling factor of non-NCQE can be reduced as the statistical sample size increases. The case with the systematic uncertainty of 10% is also calculated.

Figure 7.1 shows the expected sensitivity of discovering the DSNB signal at a 3σ significance at SK-Gd. The dashed black curve in this figure represents the sensitivity with the current uncertainty. If both the systematic uncertainties of 68% for NCQE and 36% for non-NCQE interactions are reduced to 20% (10%), the expect sensitivity will be the solid (dotted) curve in this figure. The orange dashed lines represent the several model predictions. The sensitivity will reach the predicted fluxes by reducing the uncertainties of the atmospheric neutrino event prediction. This enable us to discover DSNB at more than 3σ significance before the end of the operation of SK, which is currently planned for 2028.

7.3 Future Prospects for the Simulation Study

Background event reduction

In the excitation energy reconstruction described in Chapter 5, only the $(p, 2p)^{15}$N reaction is simulated. However, other reactions of the oxygen beam and the LH_2 target also occur in the actual measurement. A method for selecting the $(p, 2p)^{15}$N reaction from other reactions needs to be developed.

Excitation energy reconstruction

In the selection criteria describe in Sec. 5.2, the edge events that recoil protons pass through the support frame of the STRASSE are removed. It is difficult but

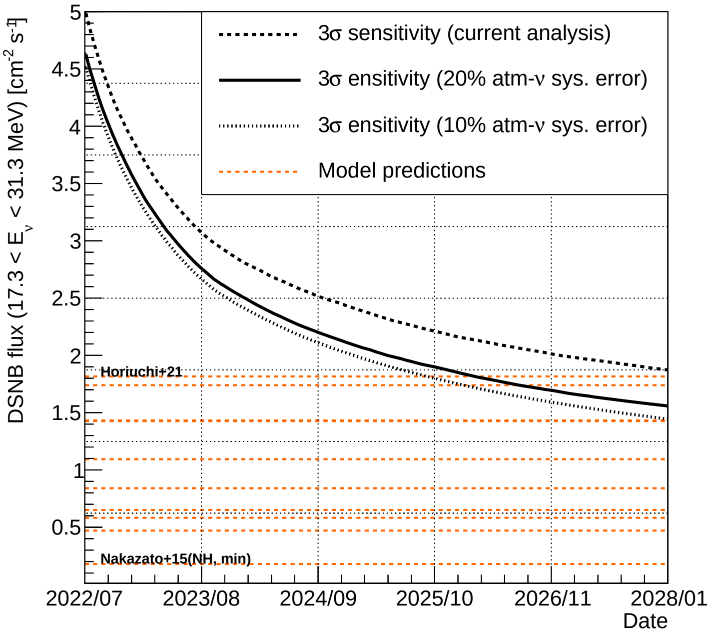

Figure 7.1: Expected sensitivity of discovering the DSNB signal at a 3σ significance at SK-Gd. The dashed black curve shows the sensitivity with the current uncertainty, while the solid (dotted) curve shows the case with 20% (10%) atmospheric neutrino systematic uncertainty. The orange dashed lines show the several major model predictions[8, 11, 6, 5, 7, 4, 3, 2, 9, 13].

possible to estimate the energy loss of the recoil proton in such an event. There are room for improving the selection efficiency of recoil protons.

The LH_2 target fills with 175 μm-thick Mylar foil. This Mylar foil contributes to the straggling and energy loss of protons and worsens the excitation energy resolution. However, it is not implemented in this simulation and this effect needs to be evaluated.

CATANA has been designed and constructed primarily for gamma-ray measurement and the energy calibration has been done by gamma-ray source. We use CATANA to detect protons, with its typical kinetic energy of $\mathcal{O}(100)$ MeV. The calibration method for such high energy region needs to be developed.

Measurement of neutron

We identify the de-excitation channels by counting the number of neutrons. There are events that miscount the number of neutrons. This effect needs to be tested.

Measurement of ^{15}O and ^{16}O

This work studied the measurement of the de-excitation process of ^{15}N. We also plan to measure ^{15}O and ^{16}O generated by the $^{16}\mathrm{O}(p,pn)^{15}\mathrm{O}$ and $^{17}\mathrm{O}(p,pn)^{16}\mathrm{O}$ reaction, respectively. A new neutron detector will be used to detect recoil neutrons in these measurements, and then further investigation is required.

7.4 Future Prospects for Improving the Neutrino-nucleus Interaction Prediction

We produces the excited state of ^{15}N, ^{15}O, and ^{16}O by the reaction between proton and oxygen nuclei. On the other hand, in the primary interaction of NCQE events, these nuclei are produced by the reaction between neutrino and oxygen nuclei. Since protons and neutrinos have different mass and spin, the energy and angular momentum of the excited states produced by proton and neutrino injections are different. These differences need to be estimated and corrected theoretically.

We also plan to measure the cross section of $^{16}\mathrm{O}(p,X)$ with various beam energies of $\mathcal{O}(100)$ MeV using the SAMURAI spectrometer. The cross section of $^{16}\mathrm{O}(n,X)$ can be estimated from that of $^{16}\mathrm{O}(p,X)$ by theoretically replacing a proton to a neutron. The $^{16}\mathrm{O}(p,X)$ and $^{16}\mathrm{O}(n,X)$ reaction occur as the secondary interaction of the atmospheric neutrino events at SK. The advantage of this inverse kinematics experiment is that we can directly detect residual nuclei and know their final state. This enable us more precise prediction of the secondary interaction.

Chapter 8

Summary

Neutrinos from supernovae offer valuable insights into physics and astrophysics. In particular, the discovery of diffuse supernova neutrino background (DSNB) would pave the way for detailed studies of the supernova explosion mechanism, the evolution of the universe, and the properties of neutrinos themselves. The Super-Kamiokande (SK) is a water Cherenkov detector and currently is the most sensitive neutrino detector in the DSNB energy region.

A barrier to discovering DSNB is the large uncertainties in the neutrino-nucleus interactions between atmospheric neutrinos and oxygen nuclei, particularly the neutral-current quasi-elastic (NCQE) interaction. A precise prediction of this atmospheric neutrino event is crucial for observing DSNB. The gamma-ray and neutron emissons from the de-excitation process of ^{15}N, ^{15}O, and ^{16}O are the key to this observation. However, the de-excitation process of these nuclei are poorly understood and experimental data are insufficient.

In order to solve this problem, we will conduct the SAMURAI-79 experiment, an inverse kinematics experiment for measuring the de-excitation process of ^{15}N, ^{15}O, and ^{16}O using the SAMURAI spectrometer at RIBF, RIKEN Nishina Center. We plan to measure the branching ratios of major de-excitation channels as a function of excitation energy of these nuclei.

In this work, we conducted a simulation study for the measurement of ^{15}N. The insights gained from this study will be applied when conducting the SAMURAI-79 experiment. First, we developed a reconstruction method for the excitation energy of ^{15}N using a setup with a newly developed detector, STRASSE. A resolution of $1.6\,\mathrm{MeV}$ (σ) in the excitation energy is achieved in this study.

Second, we studied the performance of measuring of residual nuclei and neutrons produced by the de-excitation process. The residual nuclei is identified by bending them in a magnetic field. We found that all residual nuclei can be detect by applying a magnetic field of $2.0\,\mathrm{T}$ to their trajectories. We estimated the detection efficiency of neutrons. We found that the evaporation neutrons from $^{15}\mathrm{N} \to {}^{14}\mathrm{N} + n$ reaction can be detected at a 12% efficiency using the exsisting detectors.

Then, we estimated the expected statistical performance for measuring the branching raitos. The de-excitation channels $^{14}\mathrm{N} + n$ and $^{12}\mathrm{C} + p + n$ can be measured with statistical uncertainties of 0.3% and 2.1%, respectively.

Finally, we examined the expected impact on the DSNB sensitivity at SK by improving the atmospheric neutrino event prediction. Reducing the uncertainties of the atmospheric neutrino event to 10% enable us to discover DSNB at more than 3σ significance.

Bibliography

[1] K. Nakazato et al. SUPERNOVA NEUTRINO LIGHT CURVES AND SPECTRA FOR VARIOUS PROGENITOR STARS: FROM CORE COLLAPSE TO PROTO-NEUTRON STAR COOLING. *The Astrophysical Journal Supplement Series*, 205(1):2, February 2013.

[2] S. Horiuchi et al. Impact of binary interactions on the diffuse supernova neutrino background. *Phys. Rev. D*, 103(4):043003, February 2021.

[3] Z. Tabrizi and S. Horiuchi. Flavor triangle of the diffuse supernova neutrino background. *Journal of Cosmology and Astroparticle Physics*, 2021(05):011, May 2021.

[4] D. Kresse, T. Ertl, and H.-T. Janka. Stellar Collapse Diversity and the Diffuse Supernova Neutrino Background. *The Astrophysical Journal*, 909(2):169, March 2021.

[5] S. Horiuchi et al. Diffuse supernova neutrino background from extensive core-collapse simulations of 8–100 M progenitors. *Monthly Notices of the Royal Astronomical Society*, 475(1):1363–1374, December 2017.

[6] K. Nakazato et al. SPECTRUM OF THE SUPERNOVA RELIC NEUTRINO BACKGROUND AND METALLICITY EVOLUTION OF GALAXIES. *The Astrophysical Journal*, 804(1):75, May 2015.

[7] S. Galais et al. Shock waves in supernovae: New implications on the diffuse supernova neutrino background. *Phys. Rev. D*, 81(5):053002, March 2010.

[8] Shunsaku Horiuchi, John F. Beacom, and Eli Dwek. Diffuse supernova neutrino background is detectable in Super-Kamiokande. *Phys. Rev. D*, 79(8):083013, April 2009.

[9] C. Lunardini. Diffuse Neutrino Flux from Failed Supernovae. *Phys. Rev. Lett.*, 102(23):231101, June 2009.

[10] S. Ando, K. Sato, and T. Totani. Detectability of the supernova relic neutrinos and neutrino oscillation. *Astroparticle Physics*, 18(4):307–318, 2003.

[11] M. Kaplinghat, G. Steigman, and T. P. Walker. Supernova relic neutrino background. *Phys. Rev. D*, 62(4):043001, July 2000.

[12] R. A. Malaney. Evolution of the cosmic gas and the relic supernova neutrino background. *Astroparticle Physics*, 7(1):125–136, 1997.

[13] D. H. Hartmann and S. E. Woosley. The cosmic supernova neutrino background. *Astroparticle Physics*, 7(1):137–146, 1997.

[14] T. Totani and K. Sato. Spectrum of the relic neutrino background from past supernovae and cosmological models. *Astroparticle Physics*, 3(4):367–376, 1995.

[15] K. Abe et al. Diffuse supernova neutrino background search at Super-Kamiokande. *Phys. Rev. D*, 104(12):122002, February 2021.

[16] S. Abe et al. Limits on Astrophysical Antineutrinos with the KamLAND Experiment. *The Astrophysical Journal*, 925(1):14, January 2022.

[17] M. Harada et al. Search for Astrophysical Electron Antineutrinos in Super-Kamiokande with 0.01% Gadolinium-loaded Water. *The Astrophysical Journal Letters*, 951(2):L27, July 2023.

[18] K. Abe et al. The T2K experiment. *Nuclear Instruments and Methods in Physics Research Section A: Accelerators, Spectrometers, Detectors and Associated Equipment*, 659(1):106–135, 2011.

[19] Y. Ashida. *Measurement of Neutrino and Antineutrino Neutral-Current Quasielastic-like Interactions and Applications to Supernova Relic Neutrino Searches.* PhD thesis, Kyoto University, February 2020.

[20] R. Akutsu. *A Study of Neutrons Associated with Neutrino and Antineutrino Interactions on the Water Target at the T2K Far Detector.* PhD thesis, The University of Tokyo, December 2019.

[21] M. Harada. *Development of Neutron Tagging Algorithm and Search for Supernova Relic Neutrino in SK-Gd Experiment.* PhD thesis, Okayama University, September 2023.

[22] K. Abe et al. Measurement of neutrino and antineutrino neutral-current quasielasticlike interactions on oxygen by detecting nuclear deexcitation \ensuremath\gamma rays. *Phys. Rev. D*, 100(11):112009, February 2019.

[23] S. Agostinelli et al. Geant4—a simulation toolkit. *Nuclear Instruments and Methods in Physics Research Section A: Accelerators, Spectrometers, Detectors and Associated Equipment*, 506(3):250–303, 2003.

[24] M. Yosoi. *Structures and Fragmentations of the deep-hole states in 11B and 15N.* PhD thesis, Kyoto University, 2003.

[25] T. Kobayashi et al. SAMURAI spectrometer for RI beam experiments. *Nuclear Instruments and Methods in Physics Research Section B: Beam Interactions with Materials and Atoms*, 317:294–304, 2013.

[26] H. N. Liu et al. STRASSE: a silicon tracker for quasi-free scattering measurements at the RIBF. *The European Physical Journal A*, 59(6):121, June 2023.

[27] R. Tanaka. 不安定核反応実験における高速中性子の検出, 2013.

[28] O. Benhar et al. Electron- and neutrino-nucleus scattering in the impulse approximation regime. *Phys. Rev. D*, 72(5):053005, September 2005.

[29] NIST. pstar. https://www.nist.gov/pml/stopping-power-range-tables-electrons-protons-and-helium-ions.

[30] M. Fukuda et al. *Physics and astrophysics of neutrinos*. Springer, 1994. ISBN 978-4-431-67029-2.

[31] H. Nakamura, T. Nasu, M. Sakuda, and O. Benhar. Inclusive electron spectrum in the region of pion production in electron-nucleus scattering and the effect of the quasi-elastic interaction. *Phys. Rev. C*, 76(6):065208, February 2007.

[32] Y. Ashida et al. Measurement of \ensuremath\gamma-ray production via the neutron-^16\mathrmO reaction using a 77 MeV quasimonoenergetic neutron beam. *Phys. Rev. C*, 109(1):014620, January 2024.

[33] T others Tano. Measurement of γ-Rays Generated by Neutron Interaction with 16O at 30 MeV and 250 MeV. *Progress of Theoretical and Experimental Physics*, 2024(11):113D01, October 2024.

[34] W. Hauser and H. Feshbach. The Inelastic Scattering of Neutrons. *Phys. Rev.*, 87(2):366–373, July 1952.

[35] K. Abe et al. Second gadolinium loading to Super-Kamiokande. *Nuclear Instruments and Methods in Physics Research Section A: Accelerators, Spectrometers, Detectors and Associated Equipment*, 1065:169480, 2024.

[36] Y. Hayato and L. Pickering. The NEUT neutrino interaction simulation program library. *The European Physical Journal Special Topics*, 230(24):4469–4481, December 2021.

[37] A. Boudard, J. Cugnon, J.-C. David, S. Leray, and D. Mancusi. New potentialities of the Liège intranuclear cascade model for reactions induced by nucleons and light charged particles. *Phys. Rev. C*, 87(1):014606, January 2013.

[38] IAEA-NDS. Evaluated nuclear data file (endf). https://www-nds.iaea.org/exfor/endf.htm.

[39] O. Iwamoto. Development of a Comprehensive Code for Nuclear Data Evaluation, CCONE, and Validation Using Neutron-Induced Cross Sections for Uranium Isotopes. *Journal of Nuclear Science and Technology*, 44(5):687–697, 2007.

[40] Y. Togano et al. New γ-ray detector CATANA for in-beam γ-ray spectroscopy with fast RI beams. *Nuclear Instruments and Methods in Physics Research Section B: Beam Interactions with Materials and Atoms*, 463:195–197, 2020.

[41] T. Nakamura and Y. Kondo. Large acceptance spectrometers for invariant mass spectroscopy of exotic nuclei and future developments. *Nuclear Instruments and Methods in Physics Research Section B: Beam Interactions with Materials and Atoms*, 376:156–161, 2016.

[42] Y. Kondo, T. Tomai, and T. Nakamura. Recent progress and developments for experimental studies with the SAMURAI spectrometer. *Nuclear Instruments and Methods in Physics Research Section B: Beam Interactions with Materials and Atoms*, 463:173–178, January 2020.

[43] smsimulator webpage. http://be.nucl.ap.titech.ac.jp/~nebula/simulator.php.

[44] A. Matta et al. NPTool: a simulation and analysis framework for low-energy nuclear physics experiments. *Journal of Physics G: Nuclear and Particle Physics*, 43(4):045113, March 2016.

[45] SAMURAI collaboration. Samurai magnet and detectors. https://ribf.riken.jp/SAMURAI/index.php?FrontPage.

[46] NIST. xcom. https://www.nist.gov/pml/xcom-photon-cross-sections-database.

[47] E. Ormand. YAHFC. https://github.com/LLNL/Yet-Another-Hauser-Feshbach-Code.

[48] E. Fermi. High Energy Nuclear Events. *Progress of Theoretical Physics*, 5(4):570–583, July 1950.

[49] V. F. Weisskopf and D. H. Ewing. On the Yield of Nuclear Reactions with Heavy Elements. *Phys. Rev.*, 57(6):472–485, March 1940.

[50] National Nuclear Data Center. Nudat 3.0 database. https://www.nndc.bnl.gov/nudat/.